Chapter 1
Cell-Based, Continuum and Hybrid Models of Tissue Dynamics

Hans G. Othmer

Abstract Movement of amoeboid cells is involved in embryonic development, wound repair, the immune response to bacterial invasion, and tumor formation and metastasis. Individual cells detect extracellular chemical and mechanical signals via membrane receptors, and this initiates signal transduction cascades that produce intracellular signals. These signals control the motile machinery of the cell and thereby determine the spatial localization of contact sites with the substrate and the sites of force-generation needed to produce directed motion. The coordination and control of this complex process of direction sensing, amplification of spatial differences in the signal, assembly of the motile machinery, and control of the attachment to the substratum involves numerous molecules whose spatial distribution serves to distinguish the front from the rear of the cell, and whose temporal expression is tightly controlled. How chemical and mechanical signals are integrated, how spatial differences in signals are produced, and how propulsive and adhesive forces are controlled are issues that are amenable to mathematical modeling. An overview of some approaches to these complex problems is the subject of this chapter.

1.1 Introduction

Cell and tissue movement is an integral part of many biological processes, such as large-scale tissue rearrangements or translocations that occur during embryogenesis, wound healing, angiogenesis, the immune response, and axon growth and migration. Individual cells such as bacteria migrate toward better environments by a combination of taxis and kinesis, and macrophages and neutrophils use these same processes to find bacteria and cellular debris as part of the immune response. Our understanding of signal transduction and motor control in flagellated bacteria such as *E. coli* that move by swimming and bias their movement by control of their run lengths is quite advanced [2, 93, 108] compared with our understanding of how amoeboid cells such as macrophages crawl through tissues. Some basic issues in the

---

Supported in part by NSF Grants DMS-0817529 & -1311974 and by NIH Grant GM 29123.

H.G. Othmer (✉)
School of Mathematics, University of Minnesota, Minneapolis, MN 55455, USA
e-mail: othmer@math.umn.edu

L. Preziosi et al. (eds.), *Mathematical Models and Methods for Living Systems*,
Lecture Notes in Mathematics 2167, DOI 10.1007/978-3-319-42679-2_1

latter context include how directional information is extracted from the extracellular signals, how cells develop and maintain polarity, how cells exert traction on their environment, and how adhesion to substrates or other cells is controlled.

Many eukaryotic cells can detect both the magnitude and direction of extracellular signals using receptors embedded in the cell membrane. When the signal is spatially nonuniform they may respond by directed migration either up or down the gradient of the signal, a process called taxis. When the extracellular signal is a diffusible molecule the response is chemotactic, and when it is an adhesion factor attached to the substrate or extracellular matrix (ECM) the process is called haptotaxis [1]. Cells frequently must integrate several signals downstream of the respective receptors, but the mechanisms for doing this are not well understood [45]. Chemotaxis controls the migration of single-celled organisms such as the slime mold *Dictyostelium discoideum* (Dd hereafter), toward a source of cyclic AMP (cAMP), and the movement of leukocytes toward attractants released by bacteria in a tissue. Movement toward a chemoattractant involves directional sensing and orientation, assembly of the motile machinery, polarization of the cell, and control of the attachment to the substratum or ECM. Many eukaryotic cells share common mechanisms, to be described shortly, for sensing and responding to chemoattractant gradients via G-protein-coupled receptors (GPCRs), and to adhesion gradients via integrins or their homologs.

At sufficiently high densities a cell's movement is strongly influenced by that of its neighbors. In some cases cells repeatedly form contacts with neighbors to gain traction, and then break them, only to re-attach to other nearby cells. Examples occur in the streaming and slug stages of the slime mold Dd, to be described later. In other cases cells remain attached to one another, and movement involves massive, coordinated rearrangements of entire tissues, such as folding of the neural plate to form a tube [26, 103]. Movement in both cases involves the same processes as for individual cells, with the addition of more-or-less tight coupling between the movement of neighboring cells, and we refer to both cases as tissue movement.

The classical description of amoeboid cell movement—which roughly speaking is 'crawling' movement that involves cell deformation and protrusions of various types—involves at least four different stages: protrusion, attachment to the substrate, translocation of the cell body, and detachment of the rear (Fig. 1.1) [71, 88]. (1) Cells first extend directed protrusions (lamellipodia, filopodia, or pseudopodia) at the leading edge. The force for this results from localized actin polymerization (discussed later) into cross-linked networks of filaments in lamellipodia or bundles of filaments in filopdia or pseudopodia. Behind the protrusion there is a region of actin disassembly, where filaments are disassembled, crosslinks broken and actin monomers recycled to the site of active polymerization [1]. (2) To persist, protrusions must anchor to the substrate, the extracellular matrix (ECM), or another cell via adhesive complexes, which serve as sites for molecular signaling and force transmission [91, 92]. In mesenchymal motion such as in fibroblasts, the adhesive complexes at the leading edge grow into larger focal adhesions that serve as traction 'pads' over which the cell body moves [33, 90]. (3) Next, depending on the cell type, actomyosin filaments contract at the front, in the perinuclear region, or at the

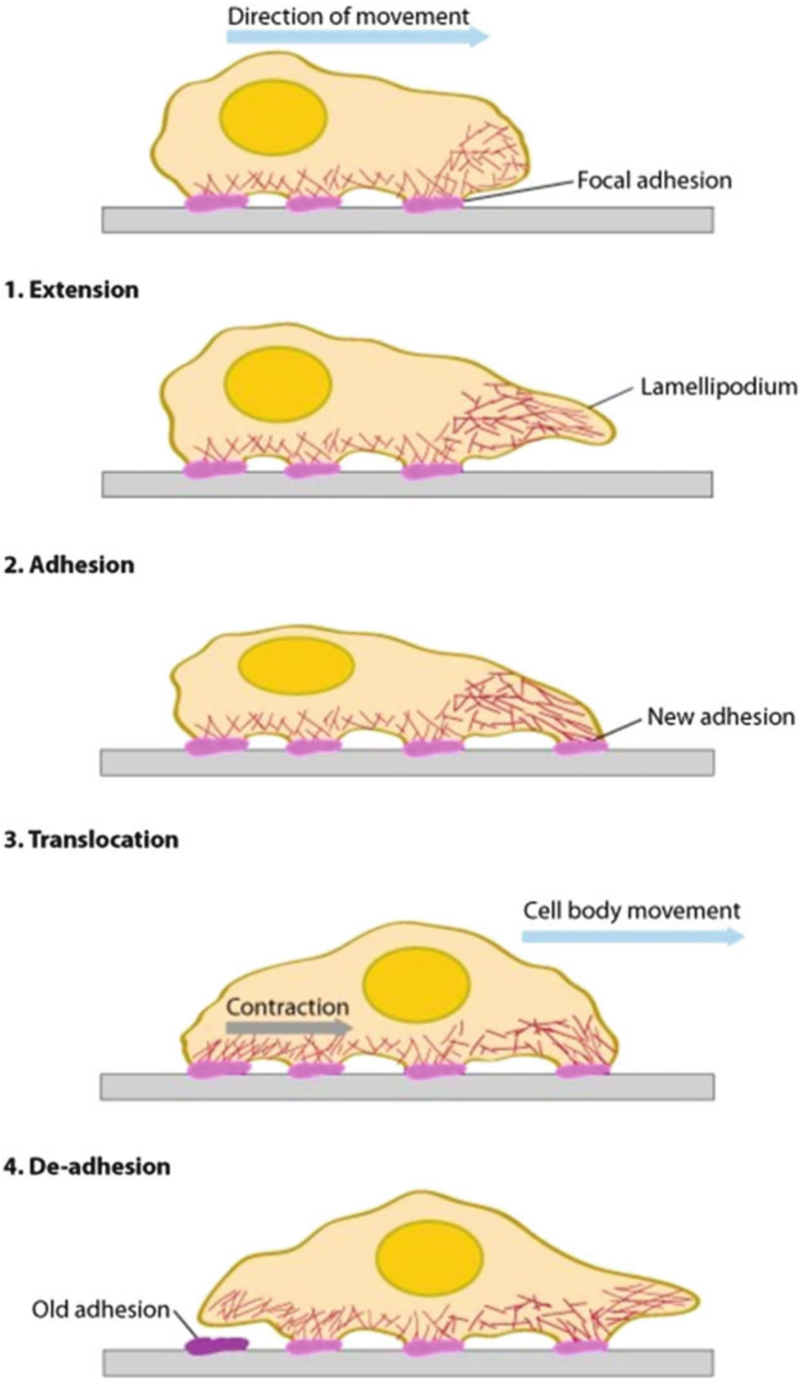

Fig. 1.1 The four stages of eukaryotic cell motion. From [3]

rear, to move the cell body forward. (4) Finally, cells release attachments at the rear [80]. In Dd or keratocytes the adhesion is weak and cells move rapidly, whereas in fibroblasts it is strong and cells move slowly.

The cytoplasm in many amoeboid cells has been characterized as a viscoelastic material whose properties are dominated by actin filaments, intermediate filaments and microtubules, collectively termed the cytoskeleton [54]. The controlled deformation and remodeling of the cytoskeleton that are involved in the shape deformations and protrusions are essential for movement. Its stress/strain response can be varied from that of a solid to that of a liquid by controlled assembly, cross-linking, and disassembly of its components. Thus the cytoskeleton is a dynamically-reorganizable nanomachine. The biochemical control processes, the microstructure of the cytoskeleton, and the formation and dissolution of adhesion sites are coordinated at the whole-cell level to produce the forces needed for movement [5, 8, 61]. Much is known about the biochemical details of the constituent steps in signaling and force generation, and the focus is now shifting to understanding whole-cell movement. For this one needs a mathematical model that links molecular-level behavior with macroscopic observations on forces exerted, cell shape, and cell speed because the large-scale mechanical effects cannot be predicted from the molecular biology of individual steps alone. However, how to formulate a multiscale model that integrates the microscopic steps into a macroscopic model is poorly understood in this context. What is needed are successively more complex model systems that will enable one to test the major modules in an integrated model sequentially. Some of these components are discussed later, and in the following section we begin with actin dynamics. However we first introduce a model system that is widely-used for both experimental and theoretical studies.

1.1.1 Dictyostelium Discoideum as a Model System

The cellular slime mold *Dictyostelium discoideum* is an important system for the study of many developmental processes, including intercellular communication, chemotaxis and differentiation. In a favorable environment the free-ranging individual amoeba feed on bacteria and divide by binary fission, but if the food supply is exhausted an elaborate developmental program is initiated (Fig. 1.2). After a period of starvation the cells attain relay competence and can respond to an external cyclic AMP signal by synthesizing and releasing cyclic AMP. This is called the relay response. The fraction of relay competent cells in a population increases with time after starvation, and at 10 h post-starvation almost all cells are relay competent [43]. At about 8 h post-starvation the cells begin aggregating in response to periodic waves of cyclic AMP initiated by randomly-located pacemaker cells. The proportion of autonomously-signaling cells in an aggregation field rises from zero at about 7 h post starvation and saturates at a small fraction of the total population within 21 h [82]. At the end of aggregation the cells form a cylindrical slug or grex which may migrate on the substrate for some time. Following migration the slug forms a fruiting

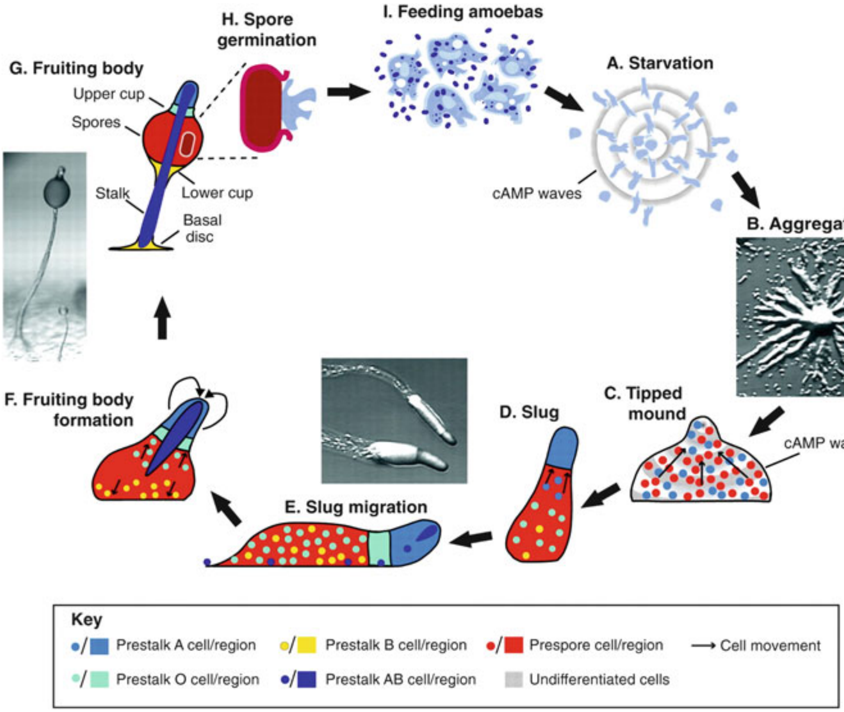

Fig. 1.2 (**a**)–(**i**) The life cycle of Dictyostelium. From [86] with permission

body, which consists of an erect stalk that supports a spherical cap containing spores. Under favorable conditions of temperature and humidity the spores are released and can germinate, and the cycle begins anew [6].

Many biological networks that occur in higher organisms first appeared in lower organisms such as Dd, and thus Dd has been widely-used for studying signal transduction, chemotaxis, and cell motility. Dd uses adenosine 3’,5’-monophosphate (cAMP) as a messenger for signaling by randomly-located pacemaker cells that emit cAMP periodically in time to control cell movement in various stages of development [74]. The production by pacemakers and relay of cAMP pulses by cells that are excitable but not oscillatory, leads to cAMP waves that propagate outward from a pacemaker, and this coupled with chemotactic movement toward the source of cAMP, facilitates the recruitment of widely-dispersed cells (Fig. 1.3). In early aggregation the cells move autonomously, but in late aggregation and in the slug stage they interact strongly and the collective motion is tissue-like [74]. In the absence of cAMP stimuli Dd cells extend protrusions called pseudopods in random directions. Aggregation-competent cells respond to cAMP stimuli by suppressing existing pseudopods and rounding up (the ’cringe response’), which occurs within about 20 s after the initial stimulus and lasts about 30 s [20]. Under uniform elevation of the ambient cAMP this is followed by extension of pseudopods in various directions, and an increase in the motility [44, 101, 105]. A localized

Fig. 1.3 Spiral cell density waves observed in aggregation. From [89] with permission

application of cAMP elicits the cringe response followed by a localized extension of a pseudopod near the point of application of the stimulus [95]. How the cell determines the direction in which the signal is largest, and how it organizes the motile machinery to polarize and move in that direction, are major questions from both the experimental and theoretical viewpoint. Since cAMP receptors remain uniformly distributed around the cell membrane during a tactic response, receptor localization or aggregation is not part of the response [55]. Well-polarized cells are able to detect and respond to chemoattractant gradients with a 2 % concentration difference between the anterior and posterior of the cell [76]. Directional changes of a shallow gradient induce polarized cells to turn, whereas large changes lead to large-scale disassembly of motile components and creation of a new 'leading edge' directed toward the stimulus [37].

The first step in developing models for the movement of individuals and population-level aggregation patterns is to identify the distinct processes involved in producing the different types of response. What a cell must do can be summarized as follows.

- Some cells (or small groups of cells) must become pacemakers. It is known from theoretical studies that a single cell suffices to create an aggregation wave [29], but this has not been demonstrated experimentally.
- A cell must detect the external cAMP and transduce it into an internal signal. A model of this process is discussed later.
- It must choose a direction in which to move and rebuild the cytoskeleton if needed to exert the necessary forces for movement.
- Cells must amplify and relay the signal, and adapt to the ambient signal.
- They must respond to an oncoming wave but not to a receding wave (this is the 'back-of-the-wave' problem), and they must move for an appropriate length of time.
- Eventually a cell interacts with its neighbors and moves collectively, first in pairs, then in streams, then in the slug and finally in the erection of the fruiting body.
- Slightly later it has to 'decide' what type of cell to become in the final fruiting body. This is a collective decision reached by the community (absent cheaters!).
- The entire aggregate has to stop migrating and erect the fruiting body.

The central theme in this chapter can be summarized in the question 'how do we model and analyze these behaviors, and what do we learn from that process?' Since there are many processes involved we approach these steps individually, and for the description of single cell behavior we modularize it as shown in Fig. 1.4.

1.2 Actin Dynamics

1.2.1 The Basic Biochemistry

Actin is a cellular protein that exists either in the globular, monomeric form, called G-actin, or in the polymeric two-stranded filament form, called F-actin. In solution G-actin can self-assemble into long filaments, into bundles, and into higher-dimensional structures. The filaments are long and flexible in vitro, and buckle easily, but in vivo cells create a dense dendritic network of short, branched filaments by tightly coupling nucleation, branching, and cross-linking of filaments in the lamellipodium, a thin (0.1–0.2 μm), sheet-like protrusion at the leading edge of a moving cell [21, 94]. Figure 1.4 shows the processes and some of the auxiliary molecules involved in vivo, and suggests the complexity of models to describe this. Table 1.1—revised from [80]—gives representative concentrations of G- and F-actin, and various auxiliary molecules.

The stiffness of the network enables new filaments to exert force on the membrane and provides the structural basis for polymerization-driven protrusion. The type of structure formed is tightly controlled by extracellular mechanical

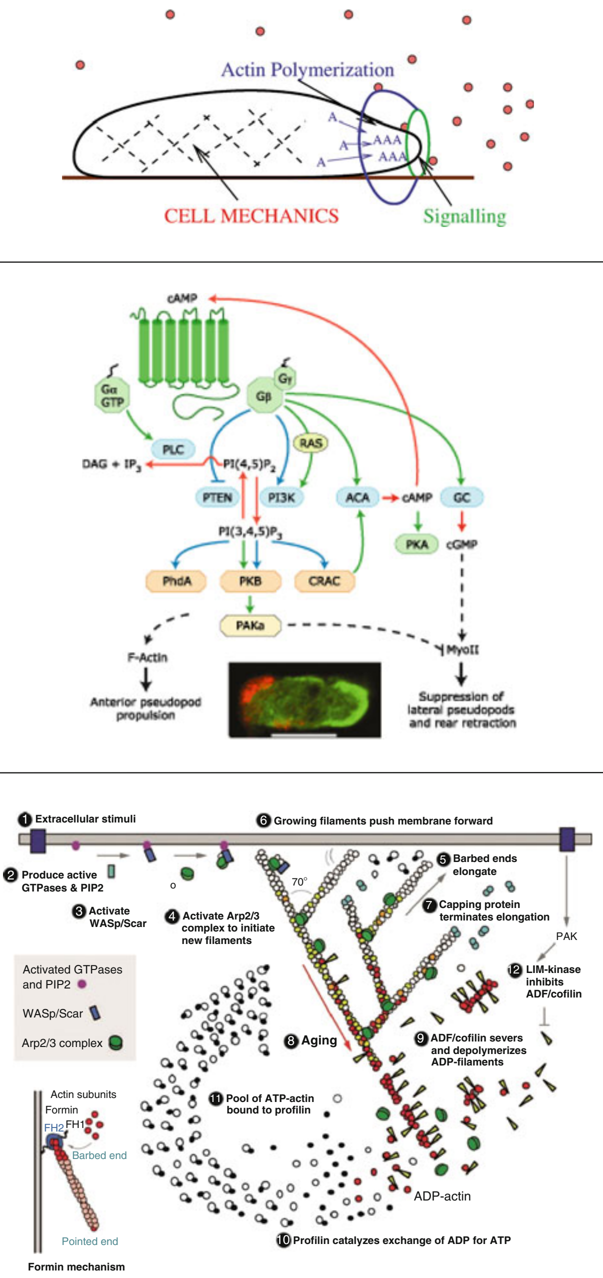

Fig. 1.4 *Top*: A schematic of the modularization of the processes involved in movement at the cell level. *Center*: A schematic of the signal transduction network that activates intracellular processes involved in movement (From [59] with permission). *Green arrows*, enzyme activation; *blue arrows*, membrane localization; *red arrows*, production and signalling; *dashed arrow*, complex regulations that have yet to be fully established. (Image) Myosin heavy chain (MHC) and actin filament distribution in polarized cells. *Lower*: The dendritic actin network, showing some of the major components involved (From [79], with permission)

Table 1.1 Concentrations in μM of actin and auxiliary molecules in various systems

Protein	Acanthamoeba	Dictyostelium	Neutrophil	Xenopus egg
Polymerized actin	100	90	100	4
Unpolymerized actin	100	160	300	12
Profilin	100			5
ADF/cofilin	20	<100		3
Arp2/3 Complex	2-4	present	1–2	

and chemical signals and by intracellular regulatory molecules. Depending on the context and the signal, a variety of motility structures can be formed, ranging from microspikes and filopdia, to larger pseudopodia and broad lamellipodia. In lamellipodia the structure of the dendritic network represents a balance between the formation of actin polymers at the leading edge, most of which occurs at the membrane, and the depolymerization of actin from the meshwork in the interior of the cell. The half-life of actin filaments in the lamellipodium ranges from around 20 s–2 min [98] and is correlated with cell speed: turnover is more rapid in rapidly-moving cells than in slower ones [66]. In any case the turnover of filaments is more than two orders of magnitude faster than the turnover of pure actin filaments in solution [111], and the in vivo system is far from thermodynamic equilibrium and under tight control. This should be contrasted with man-made polymers, which typically are static and designed for long-term stability. Additional discussion of the processes involved is given in [11].

Pollard et al. [80] provide an excellent overview of the basic issues by the series of questions around which they organize their review of the biochemistry. These serve here to provide an overview of areas in which mathematical modeling may be productive.

1. *How do cells maintain a pool of unpolymerized actin subunits?*
2. *How are signals directed to the Arp2/3 complex?*
3. *How do cells create actin filaments with free barbed ends?*
4. *How do new filaments elongate?*
5. *How do growing filaments push the membrane forward?*
6. *What limits the growth of filaments?*
7. *How are filaments marked for depolymerization?*
8. *How do filaments depolymerize?*
9. *How do stable filaments survive in the cytoplasm?*
10. *How are subunits recycled to the ATP-actin-profilin pool?*

We will not address all of these, but to these we add the question 'how do these processes balance to control the length distribution and the dynamic response?', as shown in Fig. 1.5.[1]

---

[1] Phalloidin functions by binding and stabilizing F-actin and thus this may not represent the true in vitro distribution, but later we obtain very similar distributions.

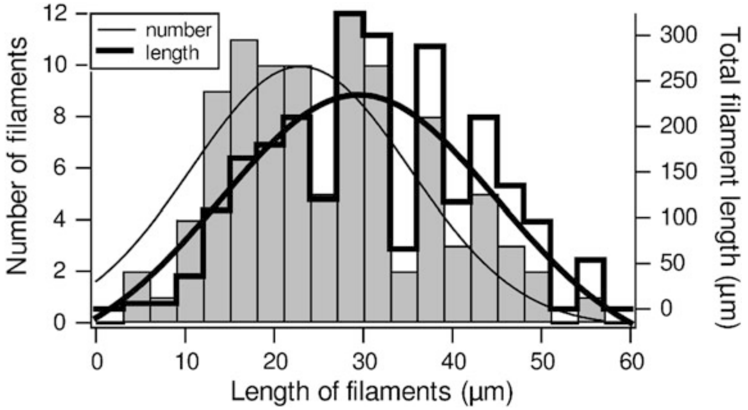

Fig. 1.5 The size distribution of actin filaments determined by fluorescence of phalloidin-rhodamine tagged actin (From [63])

In solution and in vivo G-actin can bind to either ATP (the high-energy triphosphate form) or ADP (the diphosphate form), and the phosphate group in G-ATP is slowly hydrolyzed to ADP. Thus there are three monomer types, G-ATP, G-ADP-P$_i$, and G-ADP, that can bind to a filament, and each filament is asymmetric in that the rate of monomer addition is higher at the plus (barbed) end than at the minus (pointed) end for all monomer types (see Fig. 1.6). The asymmetry of the filament stems in part from the fact that monomeric units are asymmetric themselves, having a plus and minus end.

Because nucleation of a new filament is energetically less favorable (it requires formation of a trimer, as seen later) than addition to an existing one, the tendency in an in vitro solution is to produce longer rather than more filaments. Thus some insight into the dynamics of a solution can be gotten from a simple model in which the monomers are not distinguished and only addition and release at the plus and minus ends are taken into account. At each end of a filament the reaction

$$A_m + c_m \underset{k^-}{\overset{k^+}{\rightleftarrows}} A_{m+1} \tag{1.1}$$

occurs, where A_m is the filament and c_m is the G-actin monomer concentration. If we neglect all processes but addition or release at the ends, the evolution at each end is governed by the equation

$$\frac{dA_m}{dt} = -k^+ c_m \cdot A_m + k^- A_{m+1}, \tag{1.2}$$

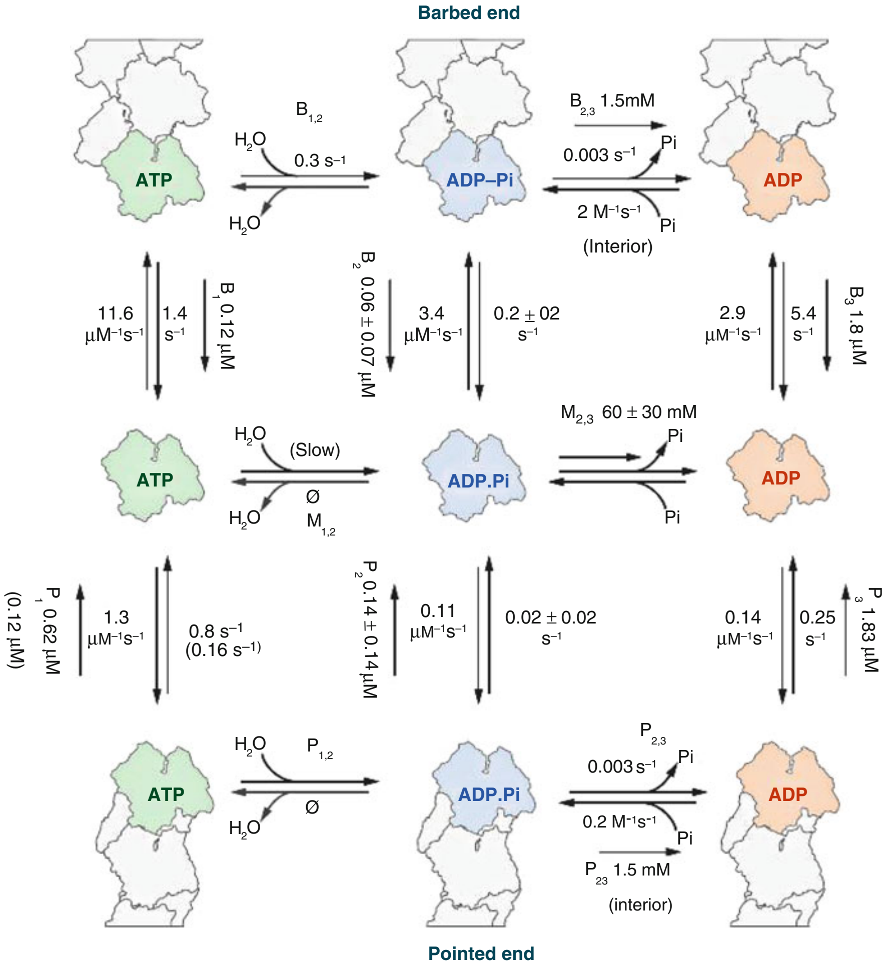

Fig. 1.6 The full set of binding rates. From [79], with permission

and therefore at equilibrium

$$K_d \equiv \frac{k^-}{k^+} = \frac{c_m \cdot A_m}{A_{m+1}} \qquad \text{or} \qquad c_m = \frac{K_d \cdot A_{m+1}}{A_m}.$$

Consequently for each given form of the monomer there is a critical concentration $c_\pm \sim K_d$ for each end of a filament at which the on- and off-rates exactly balance. Above this the filament grows at that end, while below it the end shrinks. G-ATP has a much higher on-rate at the plus end than at the minus end (cf. Fig. 1.6), and therefore the critical concentration c_+ is lower than the critical concentration c_- for the minus end. Now consider what happens as the G-actin concentration is changed.

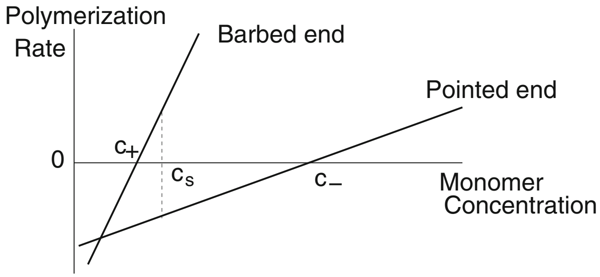

Fig. 1.7 The growth rates of plus and minus ends for G-ATP as a function of the monomer concentration

Since $c_{+} < c_{-}$, the crossover for net growth at the plus end is reached at a lower concentration than at the minus end. For any $c < c_{+}$ a filament shrinks, and for any concentration $c > c_{-}$ the filament grows. Thus there is a unique $c_{+} < c_s < c_{-}$ at which net growth at the plus end is balanced by net decay at the minus end, and the length remains constant (cf. Fig. 1.7). For this reason the process is called treadmilling at c = c_s. Note that the center of mass of the filament does not remain fixed in space during treadmilling.

In reality, the cycle consists of addition of a G-ATP at the plus end, hydrolysis of the ATP to ADP as the monomer traverses the filament, and loss of a G-ADP at the minus end. Obviously this is a highly-simplified picture, since there is a non-zero rate of addition of G-ADP at the plus end and hydrolysis is probably not obligatory. There is also a more serious problem—at physiological conditions there is about 100 μM unpolymerized actin (Table 1.1), and most of this is in the G-ATP form [84]. However, if one computes the K_d from Fig. 1.6 one sees that the K_d at both ends is much less than this, so according to Fig. 1.7, both ends grow and all actin should be polymerized. Thus there must be other factors involved, some of which are discussed next in the context of binding proteins.

1.2.2 Regulation of Polymerization, Filament Severing and Branching

Motility in amoeboid cells requires localized remodeling of actin networks at the leading edge, or formation of actin bundles in precise locations such as filopodia, and this usually involves additional proteins that regulate actin filament assembly and disassembly locally. Proteins involved in actin-filament turnover are usually localized at the leading edge and are spatially-regulated. The barbed ends of the filaments face towards the leading edge where actin assembly predominates, which leads to cycles of assembly at the front and disassembly in the rear of a lamellipodium. Electron-microscopic images of the lamellipodia of keratocytes and fibroblasts show an extensively-branched array of actin filaments [called the dendritic brush—cf. Fig. 1.4 (lower)] at the leading edge [94].

The proteins involved in local control of filament and network formation can be grouped according to their function as follows.

- Sequestering proteins: these sequester actin monomers to prevent spontaneous nucleation of filaments ($\beta-$thymosins) or interact with actin monomers to enhance nucleotide exchange (profilin).
- Crosslinking proteins: these cross-link the actin filaments and can induce a sol-to-gel transition. Examples are α-actinin. Others such as vinculin, talin, and zyxin link the actin network beneath the membrane, which is called the cortex, to the plasma membrane.
- Severing proteins: these sever F-actin to generate more filament ends for assembly or disassembly (the ADF family (actin depolymerization factor/cofilin; ADC) of proteins, gelsolin).
- Other proteins function to cap filament ends to regulate addition or loss of actin subunits (capping protein, gelsolin, the Arp2/3 complex), to nucleate filament growth (the Arp2/3 complex), or to enhance subunit dissociation by cofilin.

A schematic of how the different types of proteins affect the filaments and network structure is shown in Fig. 1.8. Their role is also illustrated in Fig. 1.4 (lower).

Despite the high concentrations of G-actin in many cells, filaments rarely nucleate spontaneously in vivo in the presence of the monomer-binding proteins profilin and thymosin-4 [80]. These sequestering proteins maintain a pool of actin ready to polymerize upon the creation of barbed ends [80], although as is seen in Table 1.1, cells such as Dd lack both, so the story may be more complex. Gelsolin

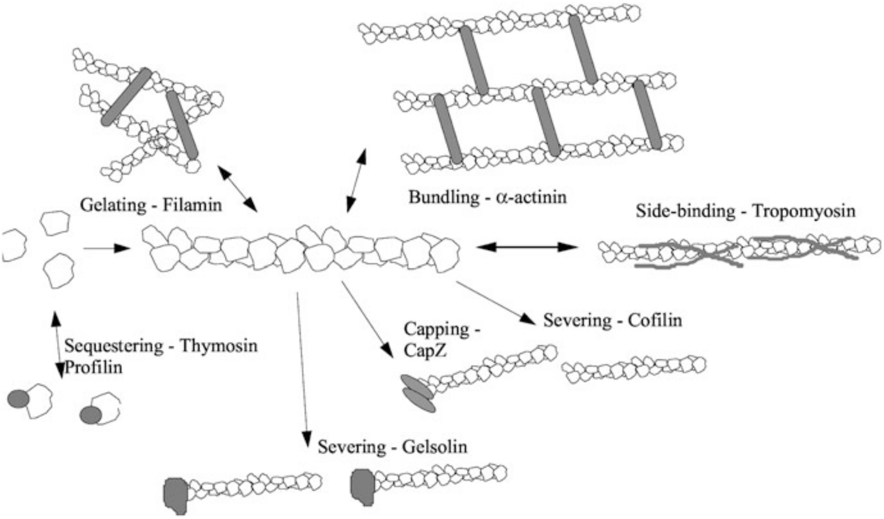

Fig. 1.8 A schematic of the effects of the various types of proteins

and other capping proteins also serve to prevent filament growth by capping the ends, as will be discussed later.

The interplay between all the factors involved produces a size distribution of actin filament lengths. One example is shown in Fig. 1.5, which is for a relatively simple situation, wherein either there is only actin monomer initially (albeit there is a protein phallodin that localizes the fluorescent label and stabilizes long filaments). Others also find an exponential length distribution under normal conditions [87], and we will see later how these can be reconciled.

1.3 A Mathematical Model for In Vitro Filament Dynamics

To gain some understanding of the evolution of the filament length distribution, we consider a closed system containing N monomers of a single type, we incorporate nucleation of filaments, and we analyze the temporal evolution of the distribution. The development here follows that in Hu et al. [47]. Let M_i denote a filament of length i and let C_i be the corresponding concentration. Of course this implicitly assumes that it makes sense to speak of concentrations, since initially there are no filaments present, but we defer until later a discussion of stochastic effects. Thus we consider the sequence

$$\underbrace{\mathcal{M}_1+\mathcal{M}_1 \underset{k_1^-}{\overset{k_1^+}{\rightleftarrows}} \mathcal{M}_2 \underset{k_2^-}{\overset{k_2^+\mathcal{M}_1}{\rightleftarrows}} \mathcal{M}_3}_{\textit{Nucleation}} \quad \underbrace{\underset{k_3^-}{\overset{k_3^+\mathcal{M}_1}{\rightleftarrows}} \mathcal{M}_4 \cdots \mathcal{M}_n \underset{k_n^-}{\overset{k_n^+\mathcal{M}_1}{\rightleftarrows}} \mathcal{M}_{n+1}\cdots}_{\textit{Propagation}}$$

Define the flux from a filament of length n-1 into a filament of length n as

$$j_n \equiv k_{n-1}^+ C_1 C_{n-1} - k_{n-1}^- C_n.$$

Then the evolution equations can be written

$$\begin{aligned}
\frac{dC_1}{dt} &= -2(k_1^+ C_1^2 - k_1^- C_2) - \textstyle\sum_{n=2}^N (k_n^+ C_1 C_n - k_n^- C_{n+1}) = -2j_2 - \sum_{n=3}^N j_n \\
&\vdots \\
\frac{dC_n}{dt} &= (k_{n-1}^+ C_1 C_{n-1} - k_{n-1}^- C_n) - (k_n^+ C_1 C_n - k_n^- C_{n+1}) = j_n - j_{n+1} \\
\frac{dC_N}{dt} &= (k_{N-1}^+ C_1 C_{N-1} - k_{N-1}^- C_N) = j_N.
\end{aligned}$$

Since the system is closed the evolution is subject to the conservation condition $\sum_{n=1}^N nC_n = C_0$, and this implies that solutions exist globally in time for any finite N.

The steady state can be found as follows. Define $K_n \equiv k_n^+/k_n^-$; then the steady state relations $j_i = 0$ lead to

$$C_n = K_{n-1}C_1C_{n-1} = K_{n-1}K_{n-2}C_1^2C_{n-2} = \cdots = \left(\prod_{i=1}^{n-1} K_i\right) C_1^n \equiv \Lambda_n C_1^n$$

and the conservation condition becomes

$$\sum_{n=1}^{N} nC_n = \sum_{n=1}^{N} n\Lambda_n C_1^n = C_0.$$

The left-hand side in the last equality is monotone increasing in C_1 and vanishes at zero, and therefore the steady-state is unique. One can also prove [47] that

- The Gibb's free energy $G = \sum_{n=1}^{N} x_n\mu_n$ is a Lyapunov function. Here the chemical potentials are defined as

  $$\mu_n = \mu_n^0(T,P) + RT\ln\frac{C_n}{C_T} = \mu_n^0(T,P) + RT\ln x_n.$$

  Further, x_n is the mole fraction of species n and C_T is the total concentration, including water. Since actin solutions are typically in the 10–100 µM range [80], we can ignore the small changes in total concentration that accompany polymerization and thus assume that C_T is constant at constant temperature and pressure. Thus the solution always converges to the steady state.
- For any fixed N >3, there exists a critical concentration C_0^* such that the profile is monotone increasing for $C_0 > C_0^*$ and $n \geq 4$, and monotone decreasing for $C_0 < C_0^*$. The critical C_0^* gives $C_1 = K^{-1}$, where $K = K_j$ for $j \geq 3$.
- For any fixed $C_0 > 0$ there exists an $N > 3$ such that the profile is monotone decreasing.

1.3.1 The Initial Evolution of the Distribution

The next objective is to understand the evolution of the length distribution in vitro. To fix the context, we stipulate that the initial condition is a pure monomer pool in a volume of 2000 μm^3, which is a typical cell size. We always the state initial conditions as concentrations, but we display the results in terms of the numbers of the different types of species. To convert between them use the fact that 1 µM corresponds to 600 molecules/μm^3; thus the total number of monomers in the standard volume used is 1.2×10^6. We know from the preceding that the final distribution is monotonic, and for these initial conditions it is monotone increasing, but the computational result in Fig. 1.10 shows that the evolution is complex. In that figure and hereafter we use rate constants from [87] given as follows.

$$k_n^+ = 10 \quad \text{for all n} \quad k_1^- = 10^6 \quad k_2^- = 10^3 \quad k_n^- = 1 \quad n \geq 3$$

Here first-order rate constants have units s^{-1} and second-order constants have units $\mu M^{-1} \cdot s^{-1}$. For these rate constants the critical concentration is 0.1 μM—above this the filaments grow and below this they shrink. Since the trimer → dimer and the dimer→ monomer steps are 3 and 6 orders of magnitude faster, resp., than other first-order steps, it is difficult to nucleate filaments in solution unless the monomer pool, and hence the forward rate k^+C_1, is sufficiently large.

To understand the evolution shown in Fig. 1.10, we lump the species into four pools, comprising monomers, dimers, trimers, and filaments of length four and longer, respectively. From this diagram one can see that different processes may balance at different stages of the evolution, as seen in Fig. 1.10. There are three distinct regimes in Fig. 1.10: the first one characterized by formation of the maximum peak height in the distribution, the second is a polymerization-driven advective phase in which the mean length increases in a wave-like movement along the length axis, and the third is a diffusive stage in which monomers are redistributed among filaments and the length distribution evolves to the steady-state distribution. The long final phase in which the profile converges to the steady state distribution is not shown in the figure.

The disparity between the off-rates for filaments of length greater than three monomers and those for dimers and trimers leads to four well-defined time scales in the early dynamics that arise from different balances in Fig. 1.9. In increasing order in the evolution they are (1) equilibration of monomers and dimers ($T_1 \sim (k_1^- + 4k^+C_1(0))^{-1} \sim \mathcal{O}(10^{-6})$ s), (2) the time at which the trimers reach their maximum ($T_2 \sim (k_2^- + 9 \cdot k_2^+ K_1 C_1(0)^2)^{-1} \sim \mathcal{O}(10^{-3})$ s), (3) establishment of the total number of filaments (T_3: $\sim$ 30 s), and (4) equilibration of the monomer pool with the filaments (T_4: to be estimated later). T_1 only plays a role in a perturbation analysis done later.

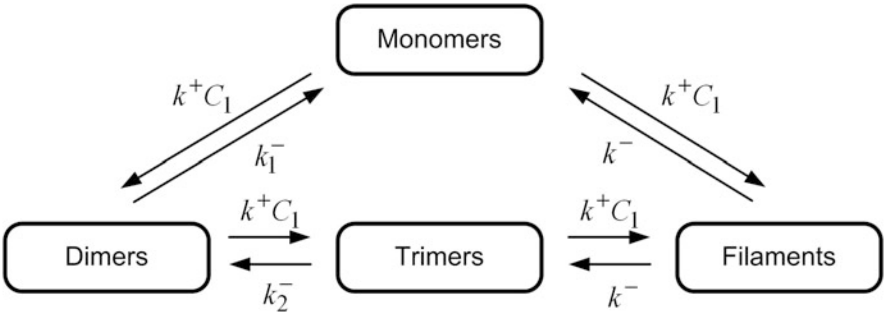

Fig. 1.9 A schematic of the network for nucleation and filament growth

On the time scale T_2 the trimer population peaks, and then dimers and trimers equilibrate with the monomer pool, whereas the slower formation of filaments can be neglected on this scale. As is shown in [47], one can truncate the steady-state equations at trimers and estimate the number of them quite accurately on this time scale. Following this, filaments are formed from the trimers, and the monomer pool decreases due to both filament formation and monomer addition to the growing filaments. In this phase the trimer concentration or number decreases monotonically, and when it reaches a level at which there is only one trimer, the total number of filaments essentially stops increasing. Of course at this point stochastic effects will play a significant role.

Once most of the trimers have been converted into filaments the total number of filaments of length at least four is fixed, and the system enters a hyperbolic phase in which the mean length of the filaments increases. This phase corresponds to the wave-like movement of the peak in the distribution (Fig. 1.10), which ends at around 30 s. This is followed by the penultimate phase in which the monomer concentration is approximately at the critical level and the number of filaments is approximately constant. In this phase there is a slow redistribution of monomers among the filaments.

To understand the hyperbolic, diffusive and terminal regimes mathematically, begin with the evolution of the filaments for $n = 4, 5, \ldots, N-1$ written as follows.

$$\begin{aligned}\frac{dC_n}{dt} &= (k_n^+ C_1 C_{n-1} - k_n^- C_n) - (k_{n+1}^+ C_1 C_n - k_{n+1}^- C_{n+1}) \\ &= -(k^+ C_1 - k^-)(C_n - C_{n-1}) + \frac{k^+ C_1 + k^-}{2}(C_{n+1} - 2C_n + C_{n-1}).\end{aligned}$$

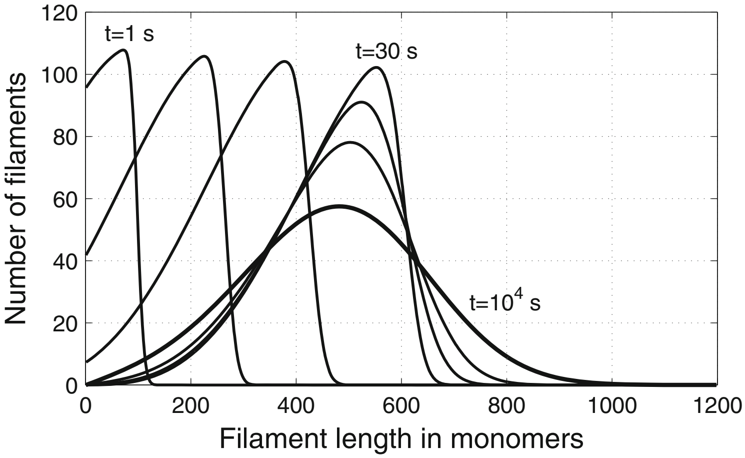

Fig. 1.10 The time evolution of the filament length distribution, starting from a G-actin concentration of 10 μM. The profiles correspond to 1, 3, 6, 30, 10^3, 3×10^3, and 10^4 s, respectively. From [47], with permission

If us denote by $C(x)$ the concentration of filaments of length $x = n\delta$ (where δ is the half length of a monomer), then we have the continuous approximation as

$$\begin{aligned}\frac{\partial C(x)}{\partial t} &= k^+ C_1 (C(x-\delta) - C(x)) - k^-(C(x) - C(x+\delta)) \\ &\approx -(k^+ C_1 - k^-)\delta \frac{\partial C}{\partial x} + \frac{k^+ C_1 + k^-}{2}\delta^2 \frac{\partial^2 C}{\partial x^2}\end{aligned}$$

and from this we see that the convective velocity is $(k^+ C_1 - k^-)$ in monomer/s, which vanishes at the critical concentration, and that the diffusion coefficient is $(k^+ C_1 + k^-)/2$ monomer^2/s. When the monomer concentration C_1 is above the critical concentration the filaments polymerize as they diffuse, at the rate $k^+ C_1 - k^-$ monomer/s, but when the monomer concentration drops to the critical value the polymerization essentially stops and diffusion dominates. Before establishment of the monomer-polymer equilibrium, convection dominates diffusion, and one observes in the computational results that the maximum of the length distribution increases at a predictable speed [47].

1.3.2 The Long-Time Evolution of the Distribution

In the final stage of the evolution the unimodal distribution evolves, albeit very slowly, into an exponential steady-state distribution. If one assumes that the monomer pool is approximately constant at the critical concentration in this phase, one has the linear system

$$\frac{dC}{dt} = \left[\begin{array}{c|c} K_1 & K_2 \\ \hline K_3 & K_4 \end{array}\right] C + \Gamma \equiv KC + \Gamma, \tag{1.3}$$

where

$$C = (C_2, C_3, \cdots,)^T \qquad \Gamma = \left(k_1^+ C_1^2, 0, \cdots 0\right)^T$$

and the $(N-1) \times (N-1)$ matrix K is given by

$$K = \left[\begin{array}{cc|ccc}
-(k^+C_1+k_1^-) & k_2^- & 0 & 0 & \cdots \\
k^+C_1 & -(k^+C_1+k_2^-) & k^- & 0 & \cdots \\
\hline
0 & k^+C_1 & -(k^+C_1+k^-) & k^- & \cdots \\
\vdots & & k^+C_1 & -(k^+C_1+k^-) & k^- \\
\vdots & & & k^+C_1 & -(k^+C_1+k^-) \\
\vdots & & & 0 & \vdots
\end{array}\right]$$

The following properties are established in [47].

- The matrix K has two large negative eigenvalues given approximately by $-k_1^-$ and $-k_2^-$, corresponding to the relaxation rate of monomers ↔ dimers and dimers ↔ trimers, respectively.
- The remaining eigenvalues are those of K_4 to lowest order. K_4 is a perturbation of a tridiagonal matrix of the form

$$K_4 = (k^+C_1)\mathbf{J} - (k^+C_1 + k^-)\mathbf{I} + k^-\mathbf{J}^T$$

  where $\mathbf{J}$ is the lower diagonal shift.
- The eigenvalues of this are

$$\lambda_p = -(k^+C_1 + k^-) + 2\sqrt{k^-k^+C_1}\cos\theta_p \qquad \theta_p \equiv \frac{p\pi}{N+1}$$

- Since $k^+ = 10, \ \ k^- = 1$, the critical concentration is $C_{1,crit} = 0.1$, it follows that

$$\lambda_p \to 0 \quad \text{as} \quad N \to \infty.$$

This shows that the slowly-evolving quasi-attractor in the diffusive stage is *not* an artifact of the assumption that the maximum filament length is finite. A more detailed spectral analysis of K shows that the slowest mode relaxes on a time scale of order of N^2, which for $N = 2000$ is of order 10^6 s [47]. This exceptionally slow relaxation provides a possible explanation for why different experiments lead to different conclusions concerning the steady-state distribution.

1.4 Stochastic Analysis of Actin Dynamics

Thus far we have modeled actin dynamics from a continuum, deterministic viewpoint, and the analysis of the resulting models gives significant insights into the evolution of filaments in solution. However, as we noted at several points, when there are only a few copies present of a particular species the deterministic model probably breaks down, and a stochastic description should be used. As we also noted previously, G-actin is present in three different forms, but to simplify the analysis we considered only one heretofore. In particular, ATP has not been singled out for any role beyond supplying the necessary energy, which is stored in some unspecified way in the filament lattice and dissipated by hydrolysis as a monomer moves from the plus to the minus end of a filament. Thus a more precise description of filament dynamics would include adding G-ATP at the plus end, hydrolysis, release of the inorganic phosphate P_i as ATP is hydrolyzed, and dissociation of G-ADP at the minus end. We deal with these issues in this section.

Actin rapidly hydrolyzes ATP upon polymerization [4] and releases bound phosphate several 100 s later [70]. ATP hydrolysis and phosphate dissociation do not cause immediate filament disassembly, but enable interaction with depolymerizing factors such as cofilin. ATP hydrolysis by actin thereby determines the overall rate of filament turnover, and some suggest that the nucleotide bound to actin filaments serves as a timer to control actin filament turnover [4].

In addition, actin filaments can be stiffened by actin-binding molecules such as the toxin phalloidin, which has been shown to delay the release of inorganic phosphate after ATP hydrolysis, i.e., the lifetime of the intermediate F-actin-ADP-Pi is significantly increased by phalloidin [25]. Thus it seems reasonable to conclude that the portion of the filament with P_i bound will be stiffer than the part following release, and this suggests that one should perhaps take position along the filament into account when considering either or both branching and severing. A summary of how some of the sequestering and severing proteins contribute to maintaining the filament length is shown in Fig. 1.11. Obviously unpolymerized actin can be sequestered in a variety of states so as to maintain a pool for rapid polymerization.

In addition to simple breakup of filaments, they can also exhibit large length fluctuations, due to the stochastic exchange of monomers between the filament and the monomer pool. Early theoretical studies on a single-monomer-type model like that used in the previous section predicted that at the steady ‘treadmilling’ state, the filament length distribution undergoes a diffusion process at the rate k^-, the off rate of monomer at filament ends [72]. However, as we showed in the previous section, the instantaneous diffusion rate constant is the mean of the polymerization and depolymerization rates. In these models both the elongation rate and diffusion constant are linear functions of monomer concentration over the entire concentration range. However, Carlier et al. showed that the growth rate of filaments can be described to first order by two distinct linear functions applicable in different regimes of monomer concentration [14]. Filaments depolymerize below

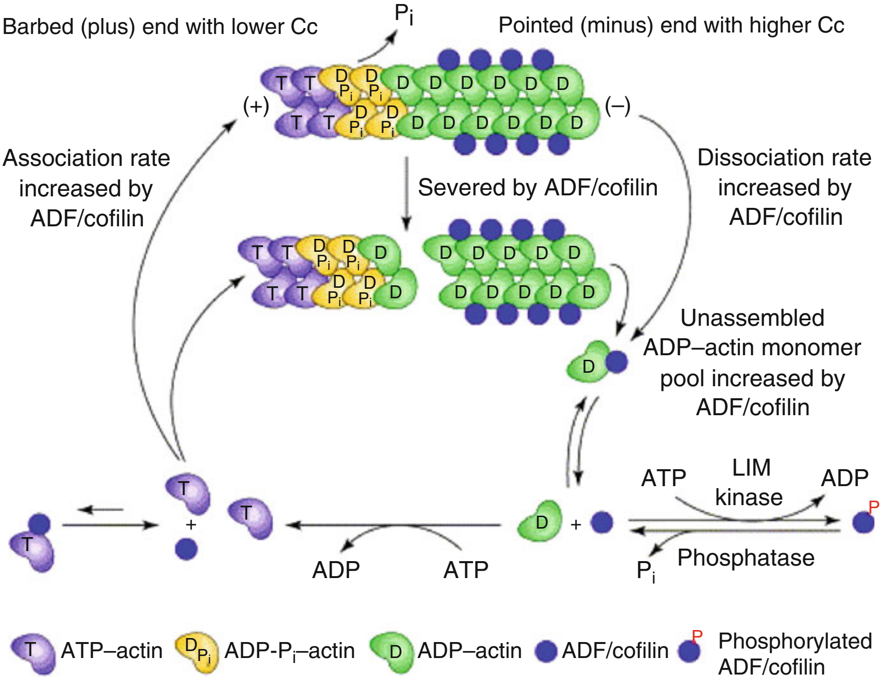

Fig. 1.11 A schematic of the effects of ADF/cofilin and profilin on filament length (From [17])

a critical concentration, whereas above it filaments grow at a constant rate and the slope of the elongation rate below the critical concentration is higher than that above it. At the critical concentration the growth rate vanishes, and filaments treadmill. In a seminal experiment, Fujiwara et al. observed that individual filaments show surprisingly large length fluctuations in the treadmilling phase [34], and other experiments confirmed this high diffusion rate [60]. A stochastic simulation that illustrates the large length fluctuations at the barbed end is shown in Fig. 1.12.

One sees there that the pointed end shrinks continuously, with relatively small fluctuations in the mean position of the end. However, there are large fluctuations at the barbed (upper) end of the filament. One sees in (b) that when the filament has an ATP cap (red) it grows, and that it decreases rapidly when the end monomer contains ADP (see inset to (b) at $\sim 232\,\mathrm{s}$). Furthermore, a significant number of ADP-Pi monomers, in which both ADP and phosphate are still bound to the protein, survive to the pointed end in this realization.

This example raises several questions, namely (1) how does one do stochastic simulations of polymer networks, and (2) what are interesting questions and what can be learned from them. Some answers to the second one are as follows.

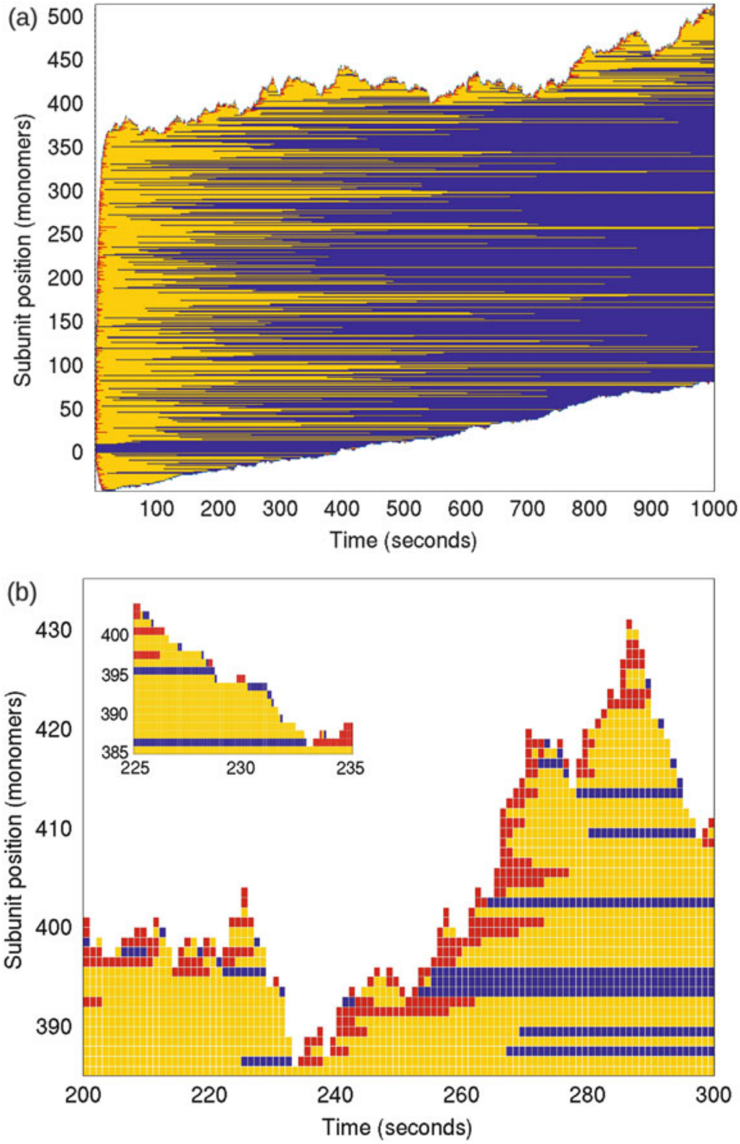

Fig. 1.12 (**a**) and (**b**) The length and nucleotide profile of a single filament during the polymerizing and treadmilling phase. Here the barbed end is at the *top* and the pointed end at the *bottom*—the former growing and the latter shrinking. *Red* represents an ATP-containing monomer, *yellow* ADP-Pi, and *blue* ADP-actin-containing monomers. Time in (**a**) and (**b**) is divided into 1-s steps, whereas in the inset to (*b*) it is divided into 0.1-s blocks. From [46] with permission

- What is the average nucleotide profile of an actin filament?
- How do different biochemical factors such as ADF/cofilin alter the average nucleotide profile and conversely, how does the nucleotide profile affect the action of these factors?
- What is the dynamic response of the distribution of length and nucleotide profiles to an "external" signal that produces an increased amount of globular actin?
- Can the types of catastrophes described above that occur near the critical concentration be explained?
- In what regimes are both the continuous and the stochastic models valid, and when must one use a stochastic model?

1.4.1 The Mathematical Description of Reaction Networks

Suppose we have a set $\mathcal{M}$ of s chemical species $\mathcal{M}_i$ that participate in a total of r reactions. We write the reactions as

$$\sum_{i}^{reac.} \nu_{ij}^{reac} \mathcal{M}_i \rightarrow \sum_{i}^{prod} \nu_{ij}^{prod} \mathcal{M}_i \qquad\qquad j = 1, \ldots r,$$

where ν_{ij} is the stoichiometric coefficient of the ith species in the jth reaction. The set of reactions gives rise to a directed graph $\mathcal{G}$ as follows. Each linear combination of reactants or products is called a complex, and each complex is identified with a vertex V_k in $\mathcal{G}$ and a directed edge E_ℓ is introduced into $\mathcal{G}$ for each reaction. The topology of $\mathcal{G}$ is encoded in its vertex-edge *incidence matrix* $\mathcal{E}$, which is defined as follows.

$$\mathcal{E}_{i\ell} = \begin{cases} +1 & \text{if } E_\ell \text{ is incident at } V_i \text{ and is directed toward it} \\ -1 & \text{if } E_\ell \text{ is incident at } V_i \text{ and is directed away from it} \\ 0 & \text{otherwise} \end{cases}$$

Suppose there p complexes—then $\mathcal{E}$ has p rows and r columns, and every column has exactly one $+1$ and one -1. Each edge carries a nonnegative weight $R_\ell(c)$ given by the intrinsic rate of the corresponding reaction. For example, the simple reaction $\mathcal{M}_1 + \mathcal{M}_2 \rightleftharpoons \mathcal{M}_3$ is written as the two steps $C(1) \rightarrow C(2)$ and $C(2) \rightarrow C(1)$, where $C(1) \equiv \mathcal{M}_1 + \mathcal{M}_2$ and $C(2) \equiv \mathcal{M}_3$. This network gives rise to the following graph and incidence matrix.

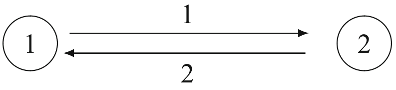

$$\mathcal{E} = \begin{bmatrix} -1 & 1 \\ 1 & -1 \end{bmatrix}$$

The evolution equation for the concentrations $(c_1, c_2)^T$ of $\mathcal{M}_1$ and $\mathcal{M}_2$ now has the factored form

$$\frac{dc}{dt} = \nu\mathcal{E}R(c), \quad c(0) = c_0 \qquad \nu \equiv \begin{bmatrix} 1 & 0 \\ 1 & 0 \\ 0 & 1 \end{bmatrix}$$

The weight functions R_j define a flow on the graph, and one says that the flow is balanced if $\mathcal{E}R(c) = 0$ [73]. In this case the fluxes entering and leaving each vertex are balanced and the solution can be represented in terms of cycles in the graph. Similar statements apply in general. For a network governed by ideal mass-action kinetics the composition $(c_1, c_2, \cdots, c_s)^T$ satisfies the evolution equations

$$\frac{dc}{dt} = \nu\mathcal{E}R(c), \quad c(0) = c_0 \tag{1.4}$$

where

$$R_\ell(c) = k_\ell P_j(c) = k_\ell \prod_{i=1}^{s} c_i^{\nu_{ij}}$$

This class of kinetics is called vertex-controlled, because the flows on an edge are controlled by the composition of the complex at the source vertex

One can also describe the evolution of a reacting system in terms of the number of molecules present for each species. Let $n = (n_1, n_2, \ldots, n_s)$ denote the discrete composition vector whose ith component n_i is the number of molecules of species $\mathcal{M}_i$ present in the volume V. This is related to the composition vector c by $n = \mathcal{N}_A Vc$, where $\mathcal{N}_A$ is Avagadro's number, and although the n_i take discrete values, they are regarded as continuous when large numbers are present. Thus the deterministic evolution for n is

$$\frac{dn}{dt} = \nu\mathcal{E}\tilde{\mathcal{R}}(n) \tag{1.5}$$

where $\tilde{\mathcal{R}}(n) \equiv \mathcal{N}_A VR(n/\mathcal{N}_A V)$. In particular, for ideal mass-action kinetics

$$\tilde{\mathcal{R}}_\ell(n) = \mathcal{N}_A Vk_\ell P_j(n/\mathcal{N}_A V) \tag{1.6}$$

$$= \mathcal{N}_A Vk_\ell \prod_{i=1}^{s} \left(\frac{n_i}{\mathcal{N}_A V}\right)^{\nu_{ij}} = \frac{k_\ell}{(\mathcal{N}_A V)^{\sum_i \nu_{ij} - 1}} \prod_{i=1}^{s} (n_i)^{\nu_{ij}} \tag{1.7}$$

$$= = \hat{k}_\ell \prod_{i=1}^{s} (n_i)^{\nu_{ij}}. \tag{1.8}$$

This is still a deterministic description, and in a stochastic description the numbers of the individual components are followed in time and the reactions are modeled as a continuous-time Markov jump process. Let $N_i(t)$ be a random variable that represents the number of molecules of species $\mathcal{M}_i$ at time t, and let N denote the vector of N_is. Let $P(n,t)$ be the joint probability that $N(t) = n$, i.e., $N_1 = n_1, N_2 = n_2, \ldots, N_s = n_s$. Clearly the state of the system at any time is now a point in $\mathcal{Z}_0^s$, where $\mathcal{Z}_0$ is the set of nonnegative integers. Formally the master equation that governs the evolution of P is

$$\frac{d}{dt}P(n,t) = \sum_{m \in \mathcal{S}(n)} \mathcal{R}(m,n) \cdot P(m,t) - \sum_{m \in \mathcal{T}(n)} R(n,m) \cdot P(n,t) \tag{1.9}$$

where $\mathcal{R}(m,n)$ is the probability per unit time of a transition from state m to state n, $\mathcal{R}(n,m)$ is the probability per unit time of a transition from state n to state m, $\mathcal{S}(n)$ is the set of all states that can terminate at n after one reaction step, and $\mathcal{T}(n)$ is the set all states reachable from n in one step of the feasible reactions. The notation is meant to suggest the 'source' and 'target' states at n; one could also call $\mathcal{S}(n)$ the predecessors of state n and $\mathcal{T}(n)$ the successors of state n. The predecessor states must be positive for conversion, degradation and catalytic reactions. Similar bounds on the target states are naturally enforced by zero rates of reaction when the reactants are absent.

The sets $\mathcal{S}(n)$ and $\mathcal{T}(n)$ are easily determined using the underlying graph structure. It follows from the definition of ν and $\mathcal{E}$ that the ℓth reaction $C(j) \to C(k)$ induces a change $\Delta n^{(\ell)} = \nu \mathcal{E}_{(\ell)}$ in the number of molecules of all species after one step of the reaction, where subscript ℓ denotes the ℓth column. Therefore the state $m = n - \nu\mathcal{E}_{(\ell)}$ is a source or predecessor to n under one step of the ℓth reaction. Similarly, states of the form $m = n + \nu\mathcal{E}_{(\ell)}$ are reachable from n in one step of the ℓth reaction. Once the graph of the network and the stoichiometry are fixed, we can sum over reactions rather than sources and targets, and consequently the master equation takes the form

$$\frac{d}{dt}P(n,t) = \sum_{\ell} \mathcal{R}_\ell(n - \nu\mathcal{E}_{(\ell)}) \cdot P(n - \nu\mathcal{E}_{(\ell)}, t) - \sum_{\ell} \mathcal{R}_\ell(n) \cdot P(n,t) \tag{1.10}$$

However, the transition probabilities $\mathcal{R}_\ell(n)$ are not simply the macroscopic rates $\tilde{\mathcal{R}}_\ell(n)$ if the reactions are second-order (or higher), because as Gillespie [41] and others have noted, combinatorial effects may play a significant role when the number of molecules is small. Hereafter we restrict attention to mass-action kinetics, and we suppose that the ℓth reaction involves conversion of the jth to the kth complex: $C(j) \to C(k)$. Then using Gillespie's notation, we can write,

$$\mathcal{R}_\ell = c_\ell h_{j(\ell)}(n) \tag{1.11}$$

where c_ℓ is the probability per unit time that the molecular species in the jth complex react, $j(\ell)$ denotes the reactant complex for the ℓth reaction, and $h_{j(\ell)}(n)$ is the number of independent combinations of the molecular components in this complex. Thus

$$c_\ell = \frac{k_\ell}{(\mathcal{N}_A V)^{\sum_i \nu_{ij(\ell)}-1}} = \hat{k}_\ell \tag{1.12}$$

and

$$h_{j(\ell)} = \prod_i \binom{n_i}{\nu_{ij(\ell)}}. \tag{1.13}$$

In the definition of h we use the standard convention that $\binom{n}{0} = 1$.

The master equation (1.10) is not solvable in general, and it is generally even difficult to obtain a closed set of equations for the moments of the distribution $P(n,t)$ when the network involves bimolecular reactions, since the evolution equation for a kth-order moment typically involves higher-order moments [36]. However, for linear reaction systems one can solve for first and second moments explicitly (modulo solving a spectral problem) and one can do this in a distributed system governed by a reaction-diffusion equation that is discretized in space [35, 56].

Remark 1 In the deterministic description of a reacting system the existence of a compact invariant set implies that solutions are bounded and exist globally in time, but the deterministic invariant set may have no significance in the stochastic description. However, the probabilities of very large numbers of species can be very small.

Consider the simple process $\phi \xrightarrow{k_1} A \xrightarrow{k_2} \phi$, and let $p_n(t)$ be the probability of having n molecules of A in the system at time t. Let $\Omega = exp(-k_2 t)$; then

$$p_n(t) = \frac{1}{k_2 n!}\left(\frac{k_1}{k_2}\right)^{n-1} (1-\Omega)^{n-1}\left(k_1(1-\Omega)^2 + k_2 n\Omega\right)\cdot exp\left(-\frac{k_1}{k_2}(1-\Omega)\right)$$

Therefore the stationary distribution is a Poisson distribution given by

$$\lim_{t\to\infty} p_n(t) = \frac{1}{n!}\left(\frac{k_1}{k_2}\right)^n exp\left(-\frac{k_1}{k_2}\right),$$

Thus $p_n(t)$ is non-zero for arbitrarily large n in both the transient and stationary distributions, but it decays rapidly with n. For example, if $k_1/k_2 \sim \mathcal{O}(1)$ and $n = 25$, $p_n \sim \mathcal{O}(10^{-25})$ in the stationary distribution. Even if the stationary mean $k_1/k_2 \sim \mathcal{O}(10)$, $p_n \leq 10^{-10}$ for $n \geq\sim 50$ (one must always choose n greater than the mean in order that $p_k < p_n$ for $k > n$).

1.4.2 The Stochastic Simulation Algorithm

Since it is generally impossible to solve the master equation analytically in interesting cases, numerical simulation methods have to be used. Numerous stochastic simulation algorithms (SSAs) have been proposed since the original exact algorithms, called the first reaction method and the direct method, were formulated by Gillespie [42]. Suppose that the system volume V is well-mixed and that there are r reactions amongst s species, as before. In Gillespie's notation, the probability density for reaction type ℓ is

$$p_\ell(\tau) = h_\ell c_\ell e^{-\sum_{i=1}^{r} h_i c_i \tau} = a_\ell e^{-a_0 \tau} \tag{1.14}$$

where

$$a_\ell = c_\ell h_\ell, \quad a_0 = \sum_{i=1}^{r} a_i.$$

In the Monte Carlo simulation algorithm of the direct method, a basic reaction cycle comprises three steps: first, determine the waiting time for the next reaction; second, determine which reaction will occur; and lastly, update the system state to reflect changes in the species involved as reactants or products in the reaction that has occurred. Accordingly, during each cycle two random numbers $r_1, r_2 \in \mathrm{URN}[0,1]$ are generated, one of which is used to calculate the waiting time according to

$$\tau = -\frac{\ln(r_1)}{a_0} \tag{1.15}$$

and the other of which is used to determine the next reaction type ℓ according to

$$\sum_{i=1}^{j-1} a_i < r_2 \cdot a_0 \leq \sum_{i=1}^{\ell} a_i. \tag{1.16}$$

The detailed algorithm is as follows.

Gillespie's Direct Method

1. Initialization (set the initial numbers of molecules, and set $t = 0$).
2. Calculate the reaction rate functions $R_i (i = 1, \ldots, r)$.
3. Generate two random numbers r_1 and r_2 from a uniform distribution on $(0, 1)$.
4. Calculate τ as follows:

$$R_0(n) = \sum R_j(n), \qquad \tau = \frac{1}{R_0(n)} ln \frac{1}{r_1}$$

5. Determine the smallest integer n_0 that satisfies

$$\sum_{i=1}^{n_0} R_i(n) > r_2 R_0(n)$$

6. Update the states of the species to account for changes due to reaction n_0 and set $t = t + \tau$.
7. Go to 2.

For large systems the algorithm is computationally costly, especially if there is a wide disparity in the reaction rates, and many ways of optimizing the original direct method algorithm by reducing the cost of specific steps have been proposed. These include pre-ordering the reactions according to their firing frequency and recomputing only the propensities of reactions which are affected by the current reaction [13], by an optimal binning algorithm [85], or by an extended enhanced direct method used for polymer dynamics to be described next [65].

A deficiency in using the direct method or most modifications of it in simulating polymer systems is that we have to account for the fact that new 'species' are created continuously, and thus the underlying state space can change as the simulation proceeds. These new species arise from polymerization/depolymerization, fragmentation of filaments, annealing of filaments, and the hydrolysis of ATP and the release of phosphate. This has led to a new algorithm described in [65], called the MO algorithm, that is significantly faster than the direct method. A comparison of the times for the two methods is shown in Fig. 1.13. A major factor that leads to the large reduction in computational time as compared with the direct method is the use of equivalence classes of species, as described in [65].

An example of the results when the method is applied to actin filament dynamics is shown if Fig. 1.14. In that figure the simulation involves a volume of 1000 μm^3 initially containing 150 filaments, each 4 μm long. The initial actin concentration is 0.7 μM and the actin filaments are initially composed of ADP-actin monomers only, while the initial G-actin pool consists of ATP actin only. Each filament is characterized by its length and nucleotide sequence, and the state of the system is characterized by the numbers of filaments of various lengths and nucleotide sequences.The reaction channels incorporated are those mentioned above, namely, polymerization/depolymerization, fragmentation of filaments, annealing of filaments, and the hydrolysis of ATP and the release of phosphate. With respect to fragmentation, it was assumed that at each time there is an equal probability of breakage, modelled as a Poisson process, at every possible position on the filament. Larger filaments are more prone to fragmentation due to the fact they contain more locations at which fragmentation can occur.

There are many other outstanding questions to be addressed in the context of filament dynamics, and next we turn to in vivo experiments and modeling that deal with the rebuilding of the cytoskeleton following treatment that depolymerizes the actin network.

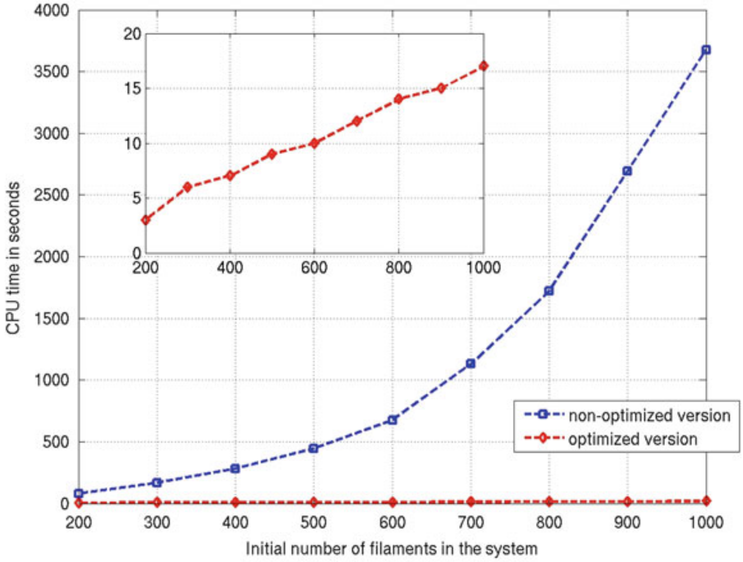

Fig. 1.13 A comparison of the computational times for the direct and modified methods. From [65] with permission

1.4.3 *Actin Wave Dynamics in Dictyostelium Discoideum*

A central question in cell motility is how a cell generates the forces necessary to produce movement by controlled remodeling of the cytoskeleton. In the absence of directional signals Dd cells explore their environment randomly, and thus the intracellular biochemical networks that control the mechanics must be tuned to produce signals that generate this random movement. Thus far there is little understanding about how the dynamic rebuilding is controlled, but some insights have been gained by observing the rebuilding of the actin network following treatment with latrunculin A (latA). LatA sequesters monomers with high affinity and leads to depolymerization of the network, and following washout of it, the rebuilding of the actin network can be observed using total internal reflection microscopy (TIRF) and confocal microscopy. TIRF targets labeled species within a thin region near the cell-substrate interface (usually less than 200 nm) and thus allows visualization of components near the surface. An example of the evolution in time of the reconstruction of the network is shown in Fig. 1.15. The waves shown in this figure only arise at those parts of the cell membrane in contact with a substrate, and thus membrane-surface interaction is essential. Actin structures in the shape of spots initially form on the ventral membrane of the substrate-attached (SA) cell, and then propagate radially in roughly circular shape with a prominent wave front and a decaying wave back [40], as seen in Fig. 1.16. TIRF imaging shows that the wave propagates not via direct transport of existing filaments, but rather, through *de*

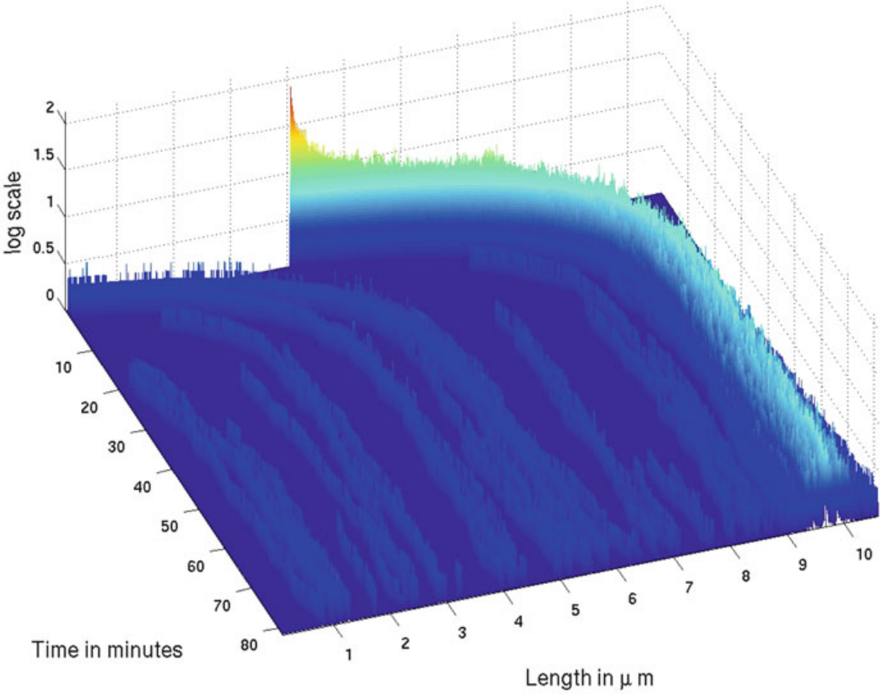

Fig. 1.14 The results of a typical simulation that includes fragmentation

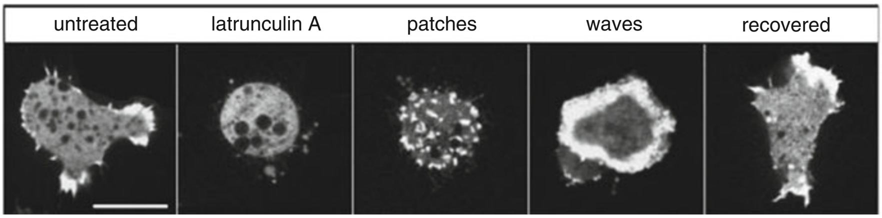

Fig. 1.15 The spatial patterns of actin network re-organization after treatment with latA and washout of the drug. The images shown, from *left to right*, are cells moving on a glass surface before the treatment with latA; cells after 16–20 min of incubation with 5 mM latA; patches that appear after the wash-out of latA; waves appear at a later stage of reorganization before normal cell shape is recovered. Patches are formed within the first 15 min after the removal of latA, waves are most abundant after 20–30 min, and recovered cells are observed after 40 min or longer. From [40] with permission

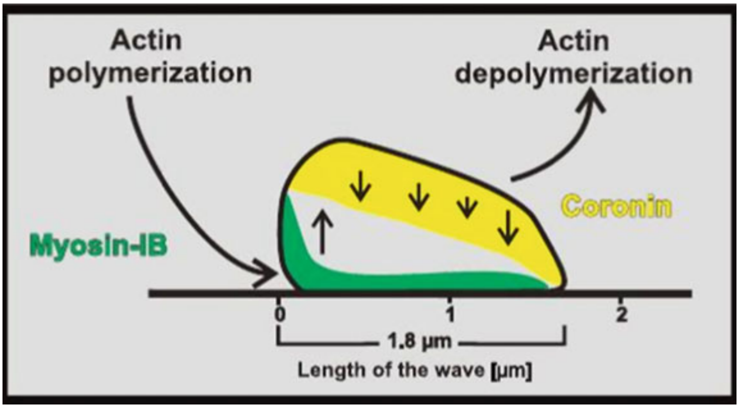

Fig. 1.16 A cross-sectional view of the actin network within a wave, showing net polymerization at the *front* and net depolymerization at the *top* and rear (From [9], with permission)

novo polymerization at the leading edge of the wave and *in situ* depolymerization at the trailing edge [40]. Imaging of the three-dimensional actin waves shows that continual growth of the actin network at the membrane pushes the network upward into the cytoplasm as shown in the schematic in Fig. 1.16.

Imaging of labeled components has identified the critical actin-binding proteins (ABP's) involved in network re-construction [9]. The actin network in the wave is believed to be dendritic, similar to that in the lamellipodium, due to the high concentration of Arp2/3 complexes measured. The Arp2/3 complex is composed of seven subunits, and can be activated by binding to nucleation-promoting factors (NPF's), G-actin and existing filaments. This interaction can lead to the formation of new filaments, in which the Arp2/3 complex caps the pointed end and attaches it to the primary filament. In latA-treated Dd cells, myosin-IB (MyoB), a single-headed motor molecule that binds to the membrane and to actin filaments in the cortex, is localized at the wave front, close to the membrane. The scaffolding protein CARMIL is probably recruited to the wave front by MyoB, and acts as an NPF for the Arp2/3 complex. In addition to CARMIL, other NPF's, such as WASP and SCAR [81], may activate Arp2/3. However, NPF's must first be activated on the membrane by binding to phospholipids. It is also observed that coronin, which is bound to filaments at the top and the back of the wave (cf. Fig. 1.16), probably destabilizes the network by removing Arp2/3 from a branch junction, thus exposing the pointed end to depolymerization [12]. A suggested schematic of these interactions is shown in Fig. 1.17 [9].

The signaling cascades that initiate and sustain the actin waves are not well-defined as yet, but a skeleton of the network has been established, and there are several distinct phases involved. The fact that waves are only initiated on membrane that is attached to a surface means that there is an unknown dependence on substrate adhesion. However, the relationship is complex, because it has been shown that a wave of activated integrin receptor follows F-actin both temporally and spatially

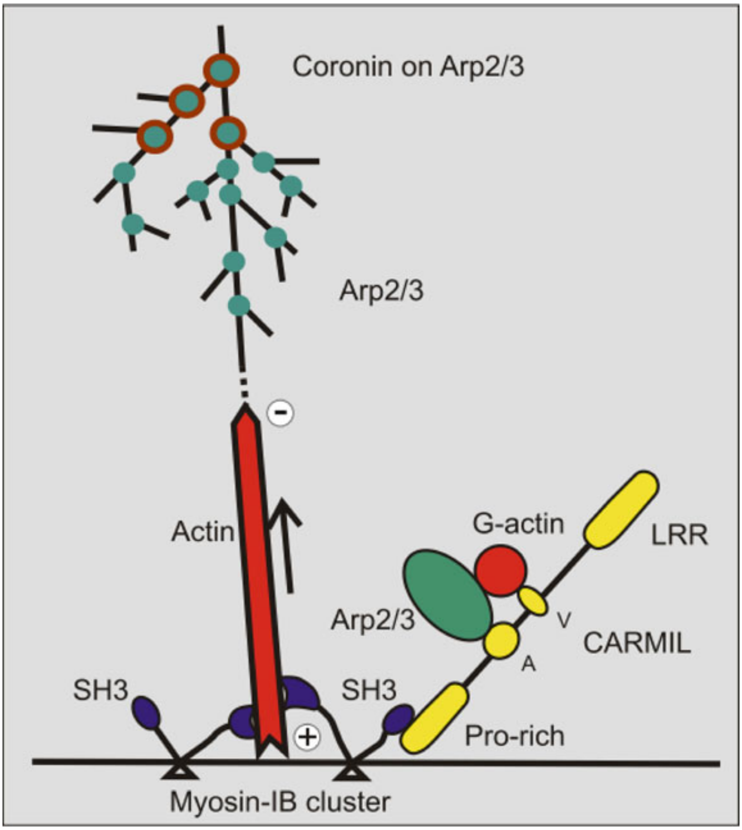

Fig. 1.17 A schematic of a suggested model for actin wave formation. The tail of Myo-IB (*blue*) binds to the plasma membrane while the motor attempts to move toward the plus end of an actin filament, which maintains attachment of the growing filament to the membrane. The head may also attach to the scaffold protein CARMIL (*yellow*), which links it to the Arp2/3 complex, where new branches are formed via Arp2/3 binding (*green*). The activity of the Arp2/3 complex is inhibited by coronin (*brown circles*). (From [9] with permission)

[15]. Thus one must construct a model that contains the essential processes, and a schematic of the model developed in [58] is shown in Fig. 1.18. That model is a continuum model and was shown to capture the essential features of the waves. However, it is too detailed for our purposes here, and we adopt a simpler scheme to describe the role of the actin network in the propagating waves. A schematic of the simplified network is shown in Fig. 1.19.

The following major assumptions have been made in the simplified model (J. Hu, V. Khamviwath, H.G. Othmer, A stochastic model for actin waves in eukaryotic cells, 2012. Unpublished manuscript).

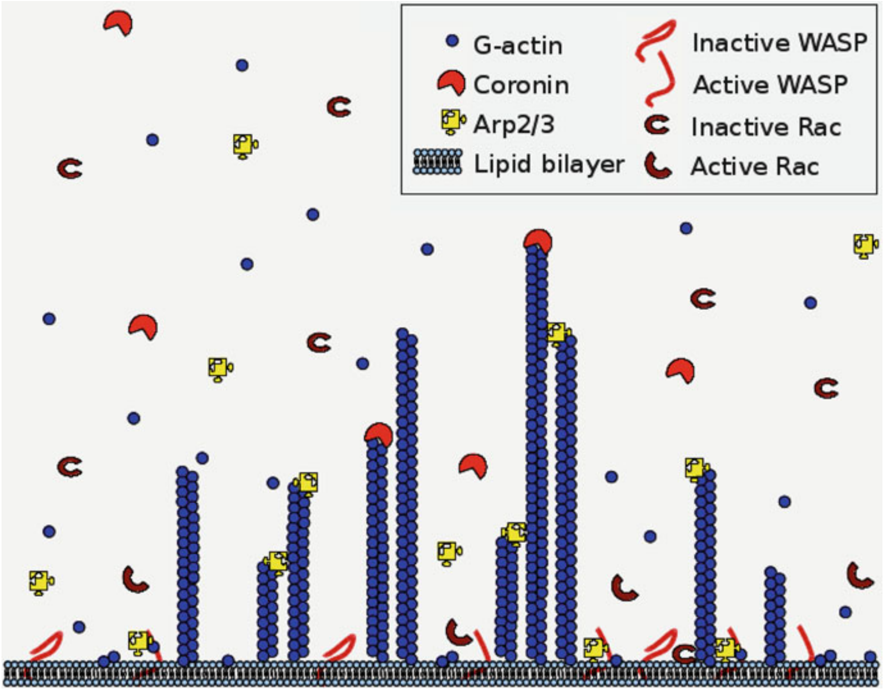

Fig. 1.18 A schematic of the stochastic model for actin waves. From [58], with permission

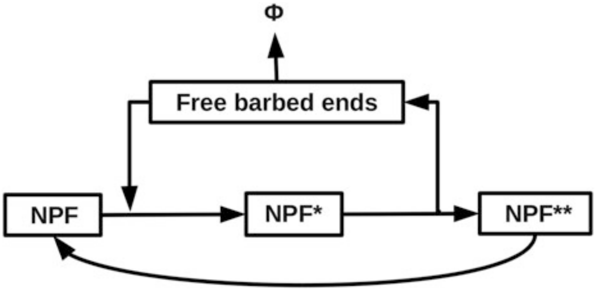

Fig. 1.19 The interconversion of the three states in the simplified model. From J. Hu, V. Khamviwath, H.G. Othmer (A stochastic model for actin waves in eukaryotic cells, 2012. Unpublished manuscript)

1. We assumed that a single molecule, NPF, in its three states is responsible for the signaling. This retains the main features of the signaling network, such as the positive feedback loop between signaling and actin dynamics.
2. The existence of an inactive state of NPF, namely NPF**, and its slow recovery to NPF controls the collapse of actin wave at the rear.

3. We assume that backbone filament nucleation sites exist on the membrane. They can generate backbone filaments, which provides a basal level of actin network on the membrane. We also assume that filament branching always requires a docking site for Arp2/3 on other filaments, either a backbone or a previously-formed branched filament.
4. NPF is activated only by free barbed ends that are in close proximity to the membrane. In other words, only active filament ends in the proximity of the membrane participate in the positive feedback.

The Mathematical Model The system domain is the rectangular solid $\Omega^{3d} = [0, L_x] \times [0, L_y] \times [0, L_z]$, where L_x, L_y, L_z are the lengths in the three axial directions. The interior of Ω^{3d} represents the cytosol, and the membrane is represented by the plane $\Omega^{2d} = [0, L_x] \times [0, L_y] \times [z = 0]$. The state variables are divided into three groups: the diffusible species in the cytosol, membrane-bound species and filament-associated species. We suppress the presence of time and space variables in equations for the evolution of the state variables unless they are needed for clarity. The definitions and values of the parameters used in the equations are defined in the next section.

The evolution of the mobile cytosolic species—G-actin (g), Arp2/3 (arp), coronin (cor) and capping proteins (cp)—are governed by

$$\begin{aligned}
\frac{\partial[g]}{\partial t} &= D_g \nabla^2[g] + \mathcal{R}_g \\
\frac{\partial[arp]}{\partial t} &= D_{arp} \nabla^2[arp] + \mathcal{R}_{p1} \\
\frac{\partial[cp]}{\partial t} &= D_{cp} \nabla^2[cp] + \mathcal{R}_{cp} \\
\frac{\partial[cor]}{\partial t} &= D_{cor} \nabla^2[cor] - \mathcal{R}_{p2} + \mathcal{R}_{p1}
\end{aligned}$$

with homogeneous Neumann boundary conditions on the surface $\partial\Omega^{3d}$ except on the membrane Ω^{2d}. On that surface the fluxes are given by

$$\begin{aligned}
-D_g \frac{\partial}{\partial z}[g]|_{z=0} &= -k^+_{bk}[g]|_{z=0} \cdot F_{bkfree} \\
&\quad -k^+_{gan}[g]|_{z=0} \cdot [npf^*\_arp] + k^-_{gan}[npf^*\_arp\_g] \\
-D_{arp} \frac{\partial}{\partial z}[arp]|_{z=0} &= -k^+_{an}[arp]|_{z=0} \cdot [npf^*] + k^-_{an}[npf^*\_arp] \\
-D_{cp} \frac{\partial}{\partial z}[cp]|_{z=0} &= -k^+_{cap}[cp]|_{z=0} \cdot F_{bkfree} \\
-D_{cor} \frac{\partial}{\partial z}[cor]|_{z=0} &= 0
\end{aligned}$$

where $\mathcal{R}$'s represent various reactions at filament ends, and F_{bkfree} the concentration of backbone filaments (J. Hu, V. Khamviwath, H.G. Othmer, A stochastic model for actin waves in eukaryotic cells, 2012. Unpublished manuscript).

The proteins that reside on the membrane are the various states of NPF's and their association with Arp2/3 and G-actin. We allow 2D diffusion for free (non-complexed) states of NPF's, but not for complexes. The dynamics of these state variables satisfy

$$\begin{aligned}
\frac{\partial[npf]}{\partial t} &= D_{npf}\nabla^2[npf] - k_{actv}F_{brfree}\cdot[npf] + k_{deg}[npf^*] + k_{recov}[npf^{**}] \\
\frac{\partial[npf^*]}{\partial t} &= D_{npf^*}\nabla^2[npf^*] + k_{actv}F_{brfree}\cdot[npf] \\
&\quad - k_{deg}[npf^*] - k_{an}^{+}[arp]|_{z=0}\cdot[npf^*] + k_{an}^{-}[npf^*\_arp] \\
\frac{\partial[npf^*\_arp]}{\partial t} &= k_{an}^{+}[arp]|_{z=0}\cdot[npf^*] - k_{an}^{-}[npf^*\_arp] \\
&\quad - k_{gan}^{+}[g]|_{z=0}\cdot[npf^*\_arp] + k_{gan}^{-}[npf^*\_arp\_g] \\
\frac{\partial[npf^*\_arp\_g]}{\partial t} &= k_{gan}^{+}[g]|_{z=0}\cdot[npf^*\_arp] - k_{gan}^{-}[npf^*\_arp\_g] \\
&\quad - k_{nucl}[npf^*\_arp\_g]\cdot F_{btot} \\
\frac{\partial[npf^{**}]}{\partial t} &= D_{npf^{**}}\nabla^2[npf^{**}] + k_{nucl}[npf^*\_arp\_g]\cdot F_{btot} - k_{recov}[npf^{**}]
\end{aligned}$$

on the domain Ω^{2d}, with zero Neumann boundary conditions at $\partial\Omega^{2d}$. The averaged concentrations of free barbed ends and total barbed ends of branched filaments within the nucleation zone adjacent to the membrane are

$$F_{brfree} = \frac{1}{L_{nucl\_zone}} \sum_{n \le \frac{2L_{nucl\_zone}}{\delta}} \left\{ \sum_{n_L, p_{tag}} f_r(n, n_L, 0, p_{tag}) \right\}$$

$$F_{btot} = \frac{1}{L_{nucl\_zone}} \left\{ \sum_{n_L} f_k(n_L) + \sum_{n \le \frac{2L_{nucl\_zone}}{\delta}} \left(\sum_{n_L, b_{tag}, p_{tag}} f_r(n, n_L, b_{tag}, p_{tag}) \right) \right\}.$$

Backbone filaments are generated on nucleation sites and remain attached to the sites until they are capped and thus considered as a member of the connected branched filaments. We assume that the latter is a rigid filament cluster, which is able to move vertically due to the polymerization at the membrane-adjacent barbed end of any member filament. The nucleation site is occupied by attached backbone filament and cannot nucleate new backbone filament until the occupied one is capped. Let S_f denote the concentration of free nucleation sites for backbone filament. These species satisfy the following equations.

$$
\begin{aligned}
\frac{\partial S_f}{\partial t} &= -\, k^+_{nuk}[g]|_{z=0} S_f + k^+_{cap}[cp]|_{z=0} \sum_{n\geq 2} f_k(n) + k^-_{nuk} f_k(1) \\
\frac{\partial f_k(1)}{\partial t} &= k^+_{nuk}[g]|_{z=0} S_f - k^-_{nuk} f_k(1) + k^-_{pk} f_k(2) - k^+_{bk}[g]|_{z=0} f_k(1) \\
\frac{\partial f_k(n)}{\partial t} &= k^+_{bk}[g]|_{z=0} f_k(n-1) + k^-_{pk} f_k(n+1) \\
&\quad - (k^+_{bk}[g]|_{z=0} + k^-_{pk}) f_k(n) - k^+_{cap}[cp]|_{z=0} f_k(n), \quad (n \geq 2)
\end{aligned}
$$

The dynamics of the branched filament is dictated by the filament-end reactions, which include the Arp2/3 removal facilitated by coronin binding and subsequent depolymerization at the pointed end, and polymerization and capping at the barbed end. The details are given in J. Hu, V. Khamviwath, H.G. Othmer (A stochastic model for actin waves in eukaryotic cells, 2012. Unpublished manuscript).

As written these equations appear to describe a continuum description, and as noted earlier, a related continuum description is analyzed in [58]. However there are generally few nucleation sites and other species may be present in low copy numbers, which suggests that a stochastic description is more appropriate. We saw earlier how this is done for a well-mixed system, and to develop an algorithm here we have to extend this to incorporate diffusion. This leads to several questions, which include (1) how does one discretize the domain correctly, and (2) how does one develop an efficient computational algorithm. The first question is answered in [57], and the second is addressed is a somewhat simpler context in [48]. A brief summary of the algorithm is as follows.

The membrane domain is partitioned into square compartments of size $l_x \times l_y$, and the cytoplasmic space into cubic compartments of size $l_x \times l_y \times l_z$, where the side lengths are all 0.1 μm. This is small enough that each compartment can be considered well-mixed. The Monte Carlo method is used to generate realizations of the stochastic model, and specifically, we implement the numerical algorithm using a modified Gillespie direct method described earlier and in [65]. In the original Gillespie direct method, two random numbers are generated for advancing the model system in each time step: one random number is used to determine the waiting time for the next reaction, and the other is used to determine which reaction type occurs [41]. In this method the reactions are distinguished by the reactants involved, and therefore, for instance, the reaction of monomer depolymerization from the pointed end of a filament of length n is considered different from that of size $n + 1$. In the MO method, the state of the systems consists of equivalence classes of filaments characterized firstly by their length, and then subdivided into classes of the same nucleotide profile. In the model developed here the nucleotide profiles play no role. Then monomer depolymerization from filaments of any size is considered as one reaction type in an equivalence class of reactants. Another reaction type consists of all the reactions involving monomer addition at a barbed end, irrespective of how long the elongating filament is, which is legitimate since the on-rate for monomer addition is independent of the filament length. Thus a third random number is needed after the reaction type that occurs is determined in order to decide which reaction within the equivalence class occurs. This treatment reduces the computational cost by 2-3 orders of magnitude by making an optimal use of the structure of the underlying reaction network (cf. [65] and Fig. 1.13).

The detailed algorithm is as follows. Suppose that the system has N_{rct_type} equivalent reaction classes and that the rate constant of the jth reaction type is r_j. Assume that there are N_{cmprt} computational compartments, in the ith of which there are RA_i^j possible reactions for reaction type j. Therefore, for the jth reaction class of the domain, the total number of this reaction in the entire domain is $RA_{tot}^j = \sum_{i=1}^{N_{cmprt}} RA_i^j$. In addition, suppose $\widehat{RA}_k^j$ denotes the total number of reactions of type j in the k-th subset in the totality of N_{sub} subsets. After setting the above system configuration, the state of the system is advanced as follows. At time t_i, the steps proceed as follows.

1. Generate a random number to determine the waiting time Δt_i for the next reaction by the reaction propensities derived from $RAtot^j$ and r_j according to the Gillespie direct method.
2. Generate a second random number, and decide which reaction type the next reaction will be from $RAtot^j$ and r_j according to the Gillespie direct method.
3. Generate a third random number and decide in which compartment the reaction type determined in Step 2 is located. In this step, instead of checking the N_{cmprt} compartment one by one, we first subdivide the compartments into subsets, determine in which subset the reacting compartment falls, and then within that subset determine the appropriate reaction compartment. In essence this is done as in step one, except that we compute total propensities within subsets and use these to determine the subset, in effect treating subsets as individual steps. (An optimization of the choice of the number of subsets is shown in Fig. 1.20.)
4. In the chosen compartment, we proceed as follows.

    - if the reactants for the chosen reaction are identical molecular species, pick any reactants to react. For example, for molecular diffusion, which molecule of the same type diffuses out of the current compartment makes no difference, since the combinatorial coefficient used in computing propensities reflects the identity of the species.
    - if the reactants are not identical molecular species, then generate another random number to decide which reactant or reactant pair to react. For example, if the pointed-end depolymerization is to occur in the reacting compartment, the filaments whose pointed end lies in the compartment may be of different lengths, and thus we must randomly choose one of these filaments.

5. Update the system configuration, and advance the time to $t_{i+1} = t_i + \Delta t_i$ where Δt_i is the random time determined in step 1. Repeat Steps 1–4 until the targeted time is reached.

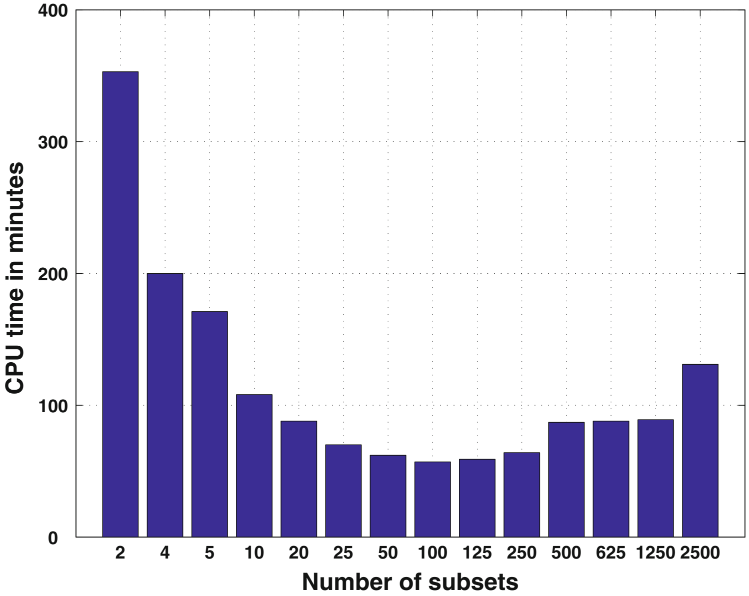

Fig. 1.20 The CPU time for a computation as a function of the number of sub-domains in the domain

The effect of subdividing of the total number of compartments in Step 3 on the computational time is shown in a simulation trial which produces the results shown in Fig. 1.20.

The stochastic model of actin assembly at the membrane, one realization of which is shown in Fig. 1.21, predicts the emergence and propagation of actin waves. In this simulation, the membrane-bound NPF partially activated at the lower left corner triggers downstream actin assembly that propagates outward as shown in the snapshot at 5.0 s in Fig. 1.21. Subsequently, the wave expands radially until it hits a boundary, where it dies. Occasionally new waves emerge spontaneously in the wake of the primary wave, as is observed experimentally. If waves are initiated at several points in the domain the waves annihilate when they meet. Thus the system has the standard characteristics of an excitable system.

One can analyze the dynamics along a line in the direction of propagation and one finds that the wave travels at about 0.1 μm/s, comparable to what is observed experimentally. Moreover, the increase in actin density at the wave front is steep, compared with the decay at the back of the wave. The F-actin level in the area well behind the wave is stabilized at about 20–25 % of that at the wave peak, consistent with the qualitative description of experimental results shown in Fig. 1.16.

While much remains to be done, some of the essential processes are embedded in the model, and some of the experimental observations can be replicated.

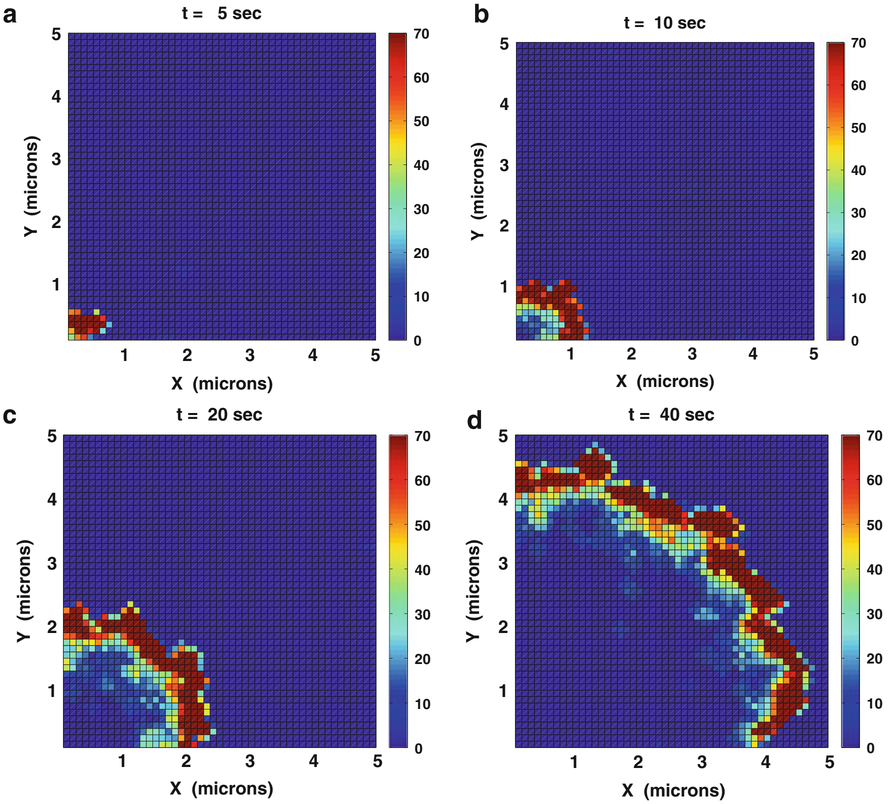

Fig. 1.21 A computational TIRF sequence for the formation and propagation of an F-actin wave. The initial G-actin concentration is 10 μM, and half of the NPF is activated at the *lower left corner*. The color index indicates the total F-actin within 100 nm of the membrane projected to each membrane compartment. The maximal density in the *color representation* is set to be 70 monomers per compartment, and thus densities larger than 70 are not distinguishable. [From J. Hu, V. Khamviwath, H.G. Othmer (A stochastic model for actin waves in eukaryotic cells, 2012. Unpublished manuscript)]

1.5 Signal Transduction, Direction Sensing and Relay

In Sect. 1.1.1 we listed the steps that a single cell must execute to successfully aggregate. These include signal detection, signal transduction, direction sensing, signal relay and movement. The mechanics of movement have not been 'solved' in previous sections, but some of the issues involved in modeling actin dynamics have been addressed. In this section we focus on the signaling aspects of the cellular response, which as was discussed earlier, centers on cAMP. Figure 1.22 shows the primary steps involved in detection, transduction, relay and the connection with the actin network. There are two main pathways in this diagram, one that leads to

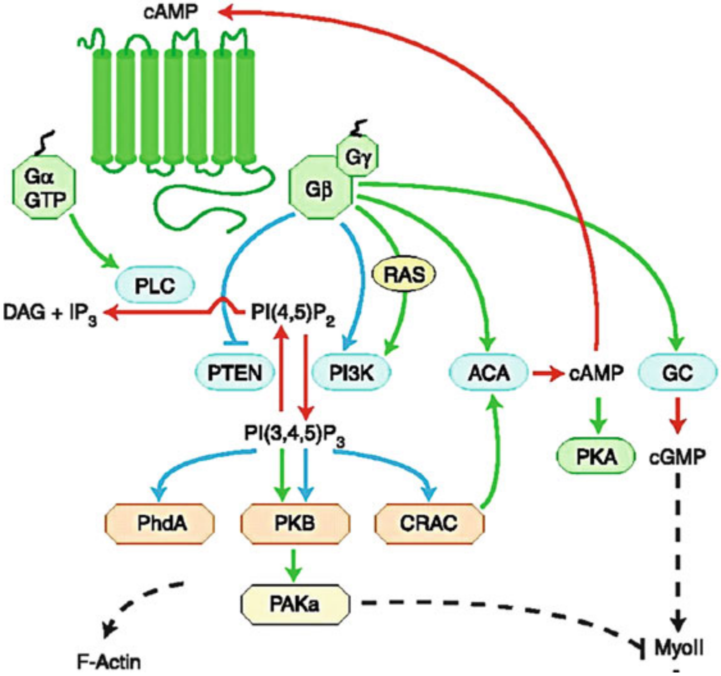

Fig. 1.22 Signal transduction in *Dictyostelium discoideum*. Modified from [59]

production of cAMP via $G_{\beta\gamma}$ and adenylyl cyclase (ACA) and secretion of cAMP—the relay response, and one that leads to modification of the cytoskeleton via $G_{\beta\gamma}$ PI3K, etc. Despite the number of components shown, the diagram only contains some of the principal actors, and we will not discuss all the components in that diagram in detail, but only those directly involved in steps considered later.

The first intracellular response to a change in extracellular cAMP is an increase in activated G proteins, catalyzed by the increase in cAMP-occupied receptors (GPCRs). G-proteins consist of an α subunit, G_α that contains a GTP/GDP binding domain as well as intrinsic GTPase activity, and a complex of a G_β and a G_γ subunit. The α and $\beta\gamma$ subunits dissociate after activation, and each can regulate the activity of different targets, including adenylyl cyclase, the enzyme that catalyzes cAMP production. A subsequent step is the generation of pleckstrin homology (PH) binding sites by the phosphorylation of the membrane lipid PtdIns(4,5)P_2 (PIP_2) by phosphoinositide 3-kinases (PI3Ks) to produce PtdIns(3,4,5)P_3 (PIP_3), which in turn is dephosphorylated to produce PtdIns(3,4)P_2 ($PI34P_2$). In Dd PIP_3 is produced by a class IA type kinase (PI3K1 and PI3K2) and a class IB type, kinase designated $PI3K_\gamma$ [19]. The former are activated via cytosolic tyrosine kinases, whereas the latter consists of a catalytic unit and a regulatory unit that is activated by $G_{\beta\gamma}$. Both PIP_3 and $PI34P_2$ provide binding sites for various cytosolic proteins containing PH domains (PHds) and recruitment is rapid: localization of PHds at the membrane peaks 5–6 s after global stimulation with cAMP [19, 49]. Both green-fluorescent-protein (GFP)-tagged CRAC (cytosolic regulator of adenylyl cyclase) and a PH_{CRAC}-GFP construct accumulate at the membrane following stimulation [32, 55]. PI3K is constitutively expressed, but both PIP_3 and $PI34P_2$ are tightly regulated by the phosphatases PTEN and SHIP, and within 10–15 s following uniform cAMP changes the PHds return to the cytoplasm, probably because the PH binding sites have been destroyed [19, 76]. This burst of PIP_3 at the membrane couples the extracellular signal to actin polymerization [52]. The level of activated G-proteins in continuously-stimulated cells reaches a stimulus-dependent level, while membrane-associated CRAC first increases, but then returns to its basal level. Therefore adaptation of the PIP_3 and cAMP responses is downstream of $G_{\beta\gamma}$ [53], and a recently-developed model shows that this occurs at the level of Ras [18], which is activated by $G_{\beta\gamma}$ (see Fig. 1.22). As is shown in Fig. 1.15, the increase in PIP_3 trails the actin increase in the developing waves, which suggests that there is a feedback from actin to the earlier steps in signal transduction shown in Fig. 1.22. Theoretical predictions as to how PI3Ks, PTEN and SHIP are spatially-regulated help in understanding how cells respond to changes in the signal [18, 58] .

Chemotactic signals also produce a rapid, transient, PI3K-dependent activation of Akt/PKB, a protein kinase that is essential for polarization and chemotaxis: mutants lacking Akt/PKB cells cannot polarize properly when placed in a chemotactic gradient and the cells move slowly [68]. Akt/PKB is activated upon recruitment to the membrane, and in Dd it activates the kinase PAKa, which regulates myosin II assembly, cortical tension, and retraction of the uropod (the tail) of the cell [19] (see Fig. 1.22). PIP_2 provides another link between signal transduction and mechanical events in that it acts as a second messenger that regulates the adhesion of the plasma membrane to the underlying cytoskeleton [67, 83].

There are a number of models for how cells extract directional information from the cAMP field. It was shown in [23], using what is in essence a model for the $G_{\beta\gamma}$-AC-cAMP part of the network in Fig. 1.22, that a cell experiences a significant difference in the front-to-back ratio of cAMP when a neighboring cell begins to signal. This shows that it is certainly possible that PI3K components in the signal-transduction pathway may also show significant front-to-back differences. Meinhardt [69] postulated an activator-inhibitor model with a third species that serves as a local inhibitor. Amplification of small external differences involves a Turing instability in the activator-inhibitor system, coupled to a slower inactivator that suppresses the primary activation. While this model produces qualitatively correct results, there is no biochemical basis for it; it is purely hypothetical and omits some of the major known processes, such as recruitment of molecules to the cell membrane from the cytosol. Several methods for achieving perfect adaptation to any extracellular signal are discussed, some of which are closely related to a simplified model of adaptation proposed earlier [74].

More recently, a model that takes into account some of the known biochemical steps, such as activation of $PI3K_\gamma$ and subsequent activation of other enzymes involved in the phosphorylation and de-phosphorylation of membrane lipids, has been proposed [62]. The positive feedback in this scheme arises from activation of PIP_2 production, but this model also ignores recruitment of most PHds to the cell membrane. A recent model based on detailed descriptions of the underlying biochemistry can replicate a variety of experimental observations that are not addressed by other models [18]. In particular, it shows that front-to-back symmetry breaking can occur at the level of Ras, and it provides a solution to the 'back-of -the-wave' problem.

The other main pathway concerns the production and secretion of cAMP, and we turn to this next. Several methods for achieving perfect adaptation to any extracellular signal are discussed in [74], and we discuss one of these in detail.

1.5.1 The Model for Signal Transduction and Relay

There are three main configurations that shed light on different aspects of a cell's response to cAMP. In the first the cells are perfused with a cAMP stream of known concentration, and the downstream level of labeled carbon is measured to determine the cell's response. These perfusion experiments, done primarily by Devreotes [27, 28], were the first to characterize the input-output response of cells. In this configuration the cAMP secreted by cells in response to the stimulus is quickly washed away, thereby precluding self-stimulation. The second configuration applies when cells are suspended in a well-mixed solution and feedback via self-stimulation occurs. Experiments of this type were done before the perfusion experiments and showed that under certain conditions the extracellular cAMP in the solution could oscillate periodically in time [39, 107]. The third configuration obtains in aggregation fields, where cells are simply plated out and allowed to develop. As shown in Fig. 1.3, complex patterns of cAMP and cell density can emerge. We shall begin with a model for the first two configurations, and then apply it to the third one.

The network for the main steps in the transduction scheme used in the model developed in [96] is shown in Fig. 1.23 and the detailed biochemical reactions are given below it.

There are three major pathways in the transduction of and adaptation to an extracellular perfusing cAMP signal ($cAMP_0$: H for short) in perfusion experiments. In the stimulus pathway H binds to GPCRs R_s, and the complex HR_s catalyzes the activation of the stimulatory G protein G_s'. This in turn binds with the inactive form of adenylate cyclase (UC) and produces the activated form of adenylate cyclase ($G_s'AC$). A GTPase activity intrinsic to the α subunit of the G protein terminates the activation. In the inhibitory pathway, an inhibitory G protein G_i' is produced by analogous steps. However, the symmetry between the pathways is broken at this point, because G_i' binds with HR_s, and in this bound form HR_s cannot activate G_s. Finally in the pathway for the production and secretion of cAMP, the activated

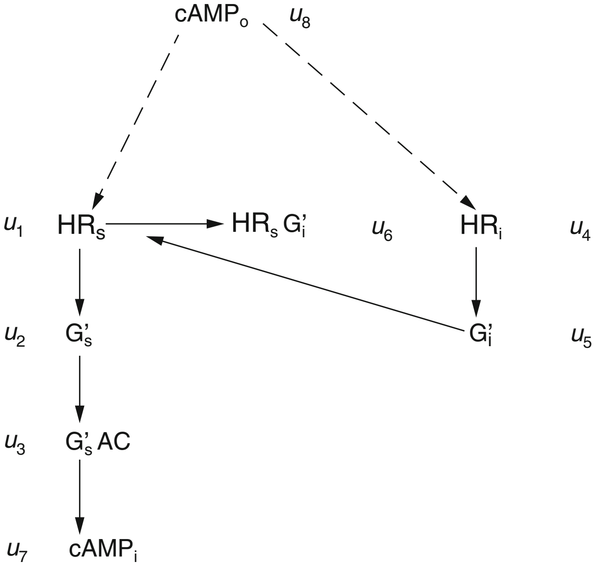

Fig. 1.23 A schematic of the interactions in the model. An extracellular cAMP stimulus serves both as the stimulus and the inhibitory signal. Adaptation arises from the action of G_i' on the cAMP-receptor complex. *Legend*: $cAMP_o$; extracellular cAMP, R_s; receptor for the stimulatory pathway, HR_s; $cAMP_o$-receptor complex, G_s'; activated stimulatory G protein, $G_s'AC$; activated form of adenylate cyclase, $cAMP_i$; intracellular cAMP, R_i; cAMP receptor in the inhibitory pathway, HR_i; cAMP-receptor complex in the inhibitory pathway, G_i'; activated form of the inhibitory G protein, HR_sG_s'; complex between HR_s and G_s'. The *symbols* u_j indicate the dimensionless concentration of that species

adenylate cyclase ($G_s'AC$) catalyzes the turnover of ATP to intracellular cAMP ($cAMP_i$). $cAMP_i$ in turn is hydrolyzed by intracellular phosphodiesterase (*iPDE*) or is secreted into the extracellular medium ($cAMP_o^*$). Here the '*' on $cAMP_o^*$ is to distinguish the secreted cAMP from the stimulatory cAMP in the perfusion solution, which is denoted by H. Further details about this model as well as kinetic parameters involved can be found in the original papers [96, 97]. The reader should note that we use G$_i'$ to activate adenylyl cyclase, which does not agree with Fig. 1.22, where $G_{\beta\gamma}$ is used. The latter is probably correct, although at the time the model was formulated this was not known. The model could easily be re-formulated to use $G_{\beta\gamma}$ as the effector in the stimulatory pathway, but this has not been done. On the inhibitory side of the pathway the best evidence is that a different G_α is used for inhibition [10], as in the model, but the details of how this is done are not known.

The steps in cAMP production and release

(I) The stimulus pathway

$$
\begin{aligned}
H + R_s &\underset{k_{-1}}{\overset{k_1}{\rightleftarrows}} HR_s\\
HR_s + G_s &\underset{k_{-2}}{\overset{k_2}{\rightleftarrows}} HR_sG_s\\
HR_sG_s + GTP &\xrightarrow{\hat{k}_3} HR_s + G'_s\\
&\qquad +GDP + \beta\gamma\\
G'_s + UC &\underset{k_{-4}}{\overset{k_4}{\rightleftarrows}} G'_sAC\\
G'_s &\xrightarrow{k_5} sGDP + P_i\\
G'_sAC &\xrightarrow{k_5} \alpha_sGDP + UC\\
&\qquad +P_i\\
\alpha_sGDP + \beta\gamma &\xrightarrow{k_6} G_s
\end{aligned}
$$

(II) The inhibitory pathway

$$
\begin{aligned}
H + R_i &\underset{h_{-1}}{\overset{h_1}{\rightleftarrows}} HR_i\\
HR_i + G_i &\underset{h_{-2}}{\overset{h_2}{\rightleftarrows}} HR_iG_i\\
HR_iG_i + GTP &\xrightarrow{\hat{h}_3} HR_i + G'_i\\
&\qquad +GDP + \beta\gamma\\
G'_i + HR_s &\underset{h_{-4}}{\overset{h_4}{\rightleftarrows}} HR_sG'_i\\
G'_i &\xrightarrow{h_5} \alpha_iGDP + P_i\\
HR_sG'_i &\xrightarrow{h_6} H + R_s + G'_i\\
HR_sG'_i &\xrightarrow{h_5} HR_s + \alpha_iGDP\\
&\qquad +P_i\\
\alpha_iGDP + \beta\gamma &\xrightarrow{h_7} G_i
\end{aligned}
$$

(III) The production and secretion of intracellular cAMP

$$
\begin{aligned}
G'_{\alpha_s}AC + ATP &\underset{l_{-1}}{\overset{\hat{l}_1}{\rightleftarrows}} G'_{\alpha_s}AC - ATP\\
G'_{\alpha_s}AC - ATP &\xrightarrow{l_2} cAMP_i + G'_{\alpha_s}AC\\
cAMP_i + iPDE &\underset{l_{-3}}{\overset{l_3}{\rightleftarrows}} cAMP_i - iPDE\\
cAMP_i - iPDE &\xrightarrow{l_4} AMP + iPDE\\
cAMP_i &\xrightarrow{l_5} cAMP^*_o
\end{aligned}
$$

This system of reactions involves fourteen species and six combinations of conserved species, and is thus described by eight independent differential equations. As we showed in [96], this model can describe the input-output behavior in the perfusion experiments very well. However, in order to better describe certain aspects of the oscillation experiments and the wave propagation studied in [97], we introduced a basal activity for the un-activated adenylate cyclase, which produces the basal cAMP concentration in the cytoplasm in the absence of an extracellular signal. The additional reaction steps introduced by the basal activity are

$$
\begin{aligned}
UC + ATP &\underset{l_{-5}}{\overset{l_5}{\rightleftarrows}} UC - ATP\\
UC - ATP &\xrightarrow{l_5^*} cAMP_i + UC.
\end{aligned}
\qquad (1.17)
$$

A second modification was to introduce a modified secretion function

$$dsr(cAMP_i) = \begin{cases} dsr_1 * cAMP_i & \text{if cAMP}_i < dsw \\ dsr_2 * (cAMP_i - dsw) + dsr_1 * dsw & \text{if cAMP}_i > dsw \end{cases} \tag{1.18}$$

and the secretion step

$$cAMP_i \xrightarrow{dsr} cAMP_o^*. \tag{1.19}$$

where dsr_1 is the basal secretion rate, dsr_2 is the active secretion rate, and dsw is the threshold concentration. The corresponding dimensionless parameters will be denoted as sr_1, sr_2, sw, and sr. The piecewise linear character of the function $dsr(\cdot)$ can introduce difficulties for certain numerical schemes that require more smoothness than C^0, and incomputations we use a smoothed version of $dsr(\cdot)$. In dimensionless form the governing equations are as follows [97].

$$\begin{aligned}
\frac{du_1}{d\tau} &= \alpha_H(\tau) - (\alpha_H(\tau) + \alpha_1)u_1 + (\beta_5 - \alpha_H(\tau))u_6 - \beta_4 u_1 u_5 \\
\frac{du_2}{d\tau} &= \alpha_2\alpha_3 c_1 u_1 - (1 + \alpha_4)u_2 - \alpha_2\alpha_3 c_1 u_1(u_2 + u_3) + \alpha_4 u_2 u_3 \\
\frac{du_3}{d\tau} &= \alpha_4 u_2 - u_3 - \alpha_4 u_2 u_3 \\
\frac{du_4}{d\tau} &= \beta_H(\tau) - (\beta_H(\tau) + \beta_1)u_4 \\
\frac{du_5}{d\tau} &= \beta_2\beta_3 c_2 u_4 - \beta_5 u_5 + \beta_6 c_3 u_6 - c_3\beta_4 u_1 u_5 - \beta_2\beta_3 c_2 u_4(u_5 + c_3 u_6) \\
\frac{du_6}{d\tau} &= -(\beta_5 + \beta_6)u_6 + \beta_4 u_1 u_5 \\
\frac{du_7}{d\tau} &= \gamma_1\gamma_2 u_3 - sr(u_7) - \gamma_4\frac{u_7}{u_7 + \gamma_3} + \gamma_5(1 - \Gamma_7 u_3) \\
\frac{du_8^*}{d\tau} &= sr(u_7)
\end{aligned} \tag{1.20}$$

To describe the dynamics of suspensions, we only have to append reactions for the extracellular dynamics and equations for the evolution of extracellular cAMP, and this leads to the additional differential equations

$$\begin{aligned}
V_o\frac{dy_{14}}{dt} &= NV_c dsr(y_{12}) + NA_c l_{-6} y_{15} + V_o l_{-8} y_{16} - NA_c l_6 y_{14} z_8 - NV_c l_8 y_{14} z_9 \\
\frac{dy_{15}}{dt} &= -(l_{-6} + l_7)y_{15} + l_6 y_{14} z_8 \\
V_o\frac{dy_{16}}{dt} &= -V_o(l_{-8} + l_9)y_{16} + NV_c l_8 y_{14} z_9.
\end{aligned} \tag{1.21}$$

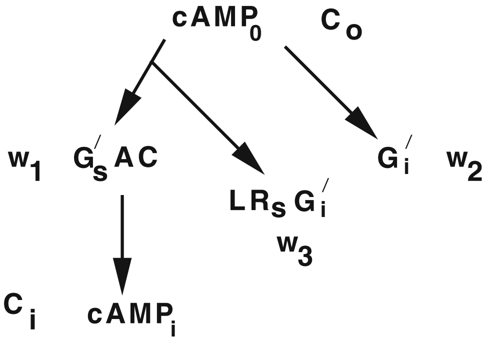

Fig. 1.24 The reduced network for the five primary variables in the reduced model. The symbols C_i, C_o and w_i i = 1,2,3 beside a species corresponds to the *symbol* used in the equations at (1.23)

Here y_{14} stands for $[cAMP_o]$, y_{15} for $[mPDE - cAMP_o]$, y_{16} for $[ePDE - cAMP_o]$, z_8 for free $[mPDE]$, z_9 for the free $[ePDE]$, V_o for the volume of the extracellular medium, V_c for the volume of a cell, A_c for the surface area of a cell, and N for the total number of cells. In addition to the differential equations, there are two other conservation equations, namely,

$$\begin{aligned} y_{15} + z_8 &= [mPDE]_T \\ y_{16} + \tfrac{NV_c}{V_o} z_9 &= \tfrac{NV_c}{V_o}[ePDE]_T \end{aligned} \tag{1.22}$$

It is clear that the newly introduced variables y_{15}, y_{16} are both positive and bounded. In fact, we have

$$0 \leq y_{15} \leq [mPDE]_T \quad 0 \leq y_{16} \leq \frac{nV_c}{V_o}[ePDE]_T.$$

It follows from this that y_{14} is also bounded.

The resulting eight-dimensional system can be further reduced by carefully analyzing the relative time variation of different components. Then, by applying a singular perturbation reduction,[2] the system can be reduced to a five-dimensional system for the variables shown in Fig. 1.24. To avoid confusion, we use the symbols w_i, C_i and C_o to denote the remaining variables, and then have the final form of the reduced system for perfusion experiments and well-mixed suspensions. In the following equations Greek letters and lower case c's represent constants. The definitions of the following parameters differ from those used earlier [97]: $L_5 = (l_{-5} + l_5^*)/(l_5[ATP])$, $\Gamma_5 = \gamma_5/(1 + L_5) = 2.4$, $L_7 = l_1/(l_{-1} + l_2)$ and $\Gamma_7 = 1 + L_7 = 1.091$; the remaining parameter values are the same as those in [97]. Many of the parameters in this model can be obtained from the literature, but the

---

[2] A brief introduction to this technique is given in Appendix.

remainder must be estimated.

$$
\begin{aligned}
\frac{dw_1}{d\tau} &= \alpha_4 u_2(1-w_1) - w_1 \\
\frac{dw_2}{d\tau} &= \beta_2\beta_3 c_2 u_4(1-w_2-c_3w_3) - \beta_5 w_2 + \beta_6 c_3 w_3 - c_3\beta_4 u_1 w_2 \\
\frac{dw_3}{d\tau} &= -(\beta_5+\beta_6)w_3 + \beta_4 u_1 w_2 \\
\frac{dC_i}{d\tau} &= \gamma_1\gamma_2 w_1 + \Gamma_5(1-\Gamma_7 w_1) - \gamma_4\frac{C_i}{C_i+\gamma_3} - sr(C_i) \\
\frac{dC_o}{d\tau} &= \frac{\rho}{1-\rho}\left(sr(C_i) - \gamma_7\frac{C_o}{C_o+\gamma_6} - \gamma_9\frac{C_o}{C_o+\gamma_8}\right).
\end{aligned}
\tag{1.23}
$$

To illustrate the interpretation of terms in these equations, consider the fourth equation, that for the change in cAMP$_i$. The first term represents the production of cAMP$_i$ via the activated cyclase, the second term represents the basal production of cAMP$_i$, the third term represents the rate at which cAMP$_i$ is degraded by PDE, and the last term represents the rate at which it is secreted. As a result of applying the singular perturbation, some rapidly-varying variables are related to others via algebraic equations. Most are eliminated completely, but it is convenient to retain some of these quantities for the purpose of explaining how the system functions. They are the fraction of R$_s$ bound, the amount of activated G$_s$, and the fraction of R$_i$ bound, which in dimensionless form are given by

$$
u_1 = \frac{\alpha_0 C_o + (\beta_5 - \alpha_0 C_o)w_3}{\alpha_1 + \alpha_0 C_o + \beta_4 w_2} \qquad u_2 = \frac{\alpha_2\alpha_3 c_1 u_1(1-w_1)}{1+\alpha_4+\alpha_2\alpha_3 c_1 u_1 - \alpha_4 w_1}
$$

$$
u_4 = \frac{\beta_0 C_o}{\beta_1 + \beta_0 C_o}.
$$

1.5.2 The Dynamics Under Imposed and Self-Generated Stimuli

A qualitative description of how this system responds to stimuli is as follows. Suppose first that cAMP$_o$ is clamped, and that the system is adapted to a given level of cAMP$_o$. A change in cAMP$_o$ is reflected in the stimulatory (inhibitory) pathway via a change in the term $\alpha_o C_o$ ($\beta_o C_o$) that appears in the fraction u_1 (u_4) of stimulatory (inhibitory) receptors bound with ligand. On the stimulatory side, this input is immediately reflected in a change in u_2 (G_s') because the activation is fast. This increases the amount of activated cyclase (w_1), and this in turn produces more *cAMP*$_i$ and the relay response. Simultaneously, but on a slightly slower time scale, the inhibitory pathway activates the inhibitory G-protein G_i, which competitively interferes with the production of G_s', and hence the activation of the cyclase. This interference then leads to adaptation in the model, and the combination of relay and adaptation qualitatively explains the response in the context of perfusion experiments. When cAMP$_o$ is not clamped a positive feedback loop is created via the secretion of cAMP$_i$. Depending on how it is tuned, this feedback system leads either to amplification of a pulse of cAMP$_o$ or to sustained oscillations. Using experimentally-determined parameters where possible, and estimates for the remaining parameters, this system predicts a time course of cAMP levels and secretion rates that agrees both qualitatively and quantitatively with experimentally-observed results in perfusion and suspension experiments.

In Fig. 1.25 we show the response to a single step change and to a four-step increase in cAMP$_o$ in a simulated perfusion experiment, using the model above developed in [97]. The response shown there is based on experimental parameters where they are known, and one sees that the system does not adapt fully at large stimuli. However this can be corrected by a simple modification of the dynamics [74]. At all stimulus levels the cAMP and secretion responses peak at about 1 min after stimulation, which is as observed experimentally [16].

In Fig. 1.26 we show the intracellular and extracellular cAMP oscillations in a suspension of cells. The amplitudes of the intracellular cAMP oscillations matches well with the experimental observations shown in the right-hand panel, but the extracellular concentration is lower. This depends on the secretion rate, the amount of the extracellular phosphodiesterase that degrades the CAMP, and other factors. Suffice it to say that the model captures the essential aspects of the cellular response, both to imposed stimuli and in suspensions, and therefore can be used to study aggregation of spatially-distributed populations.

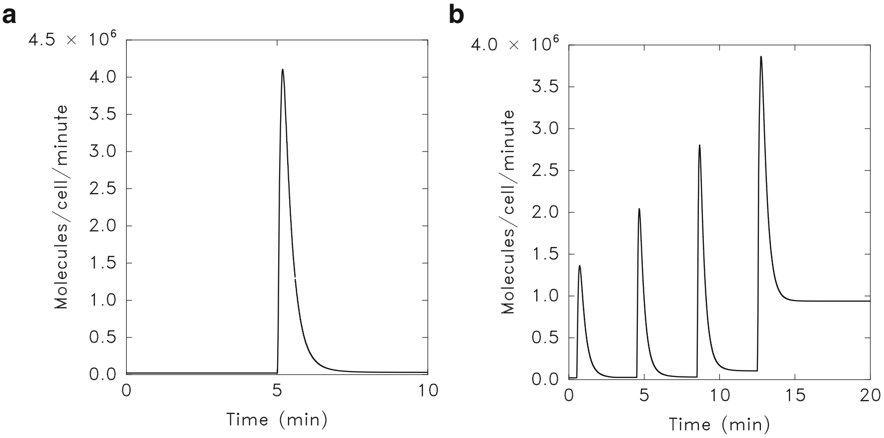

Fig. 1.25 The predicted secretion rate in response to imposed stimuli. *Left*: The response to a step from 0 to 1 μM in extracellular cAMP. *Right*: The response to a sequence of three tenfold steps from 0 to 1 μM in extracellular cAMP

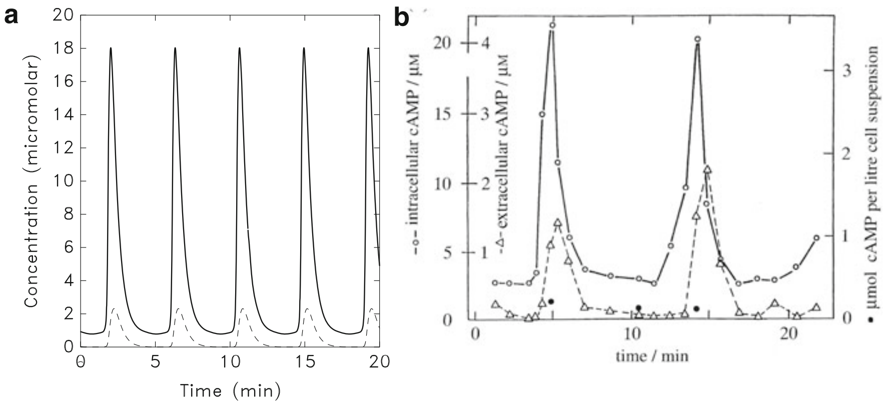

Fig. 1.26 *Left*: Periodic oscillations in a numerical simulation of suspension experiments for $\gamma_2 = 0.4$. *Solid line*: intracellular cAMP; *dashed line*: extracellular cAMP. *Right*: Experimental measurements of intracellular (*open circle*) and extracellular (*triangle*) cAMP concentration. Redrawn from Fig. 2 of Gerish and Wick [38]

1.5.3 The Reaction-Diffusion Equations for Early Aggregation

In aggregation fields the concentrations vary in space as well as time, and this leads to new phenomena. At the very least this requires a different equation for the extracellular cAMP, which can diffuse throughout space. Here one also has to decide whether to introduce a continuum density for the cells, or retain a hybrid description in which $cAMP_o$ satisfies a reaction-diffusion equation and the cells are treated as point particles. We adopt the latter description here, and this leads to the following equations. In these equations the superscript ^{i} denotes the ith cell, $\mathbf{x}_i$ denotes the spatial position of the ith cell, and the dependence of w_j^i and C_i^i on $\mathbf{x}_i$ is implicit in the equations.

$$\frac{dw_1^i}{d\tau} = \alpha_4 u_2^i - w_1^i - \alpha_4 u_2^i w_1^i$$

$$\frac{dw_2^i}{d\tau} = \beta_2\beta_3 c_2 u_4^i - \beta_5 w_2^i + \beta_6 c_3 w_3^i - c_3\beta_4 u_1^i w_2^i - \beta_2\beta_3 c_2 u_4^i (w_2^i + c_3 w_3^i)$$

$$\frac{dw_3^i}{d\tau} = -(\beta_5 + \beta_6) w_3^i + \beta_4 u_1^i w_2^i$$

$$\frac{dC_i^i}{d\tau} = \gamma_1\gamma_2 w_1^i + \Gamma_5(1 - \Gamma_7 w_1^i) - \gamma_4 \frac{C_i^i}{C_i^i + \gamma_3} - sr(C_i^i)$$

$$\frac{\partial C_o}{\partial \tau} = \Delta_1 \nabla^2 C_o(\mathbf{x}) - \hat{\gamma}_9 \frac{C_o(\mathbf{x})}{C_o(\mathbf{x}) + \gamma_8} + \sum_{i=1}^{N} \frac{V_c}{V_o} \delta(\mathbf{x} - \mathbf{x}_i) \left(sr(C_i^i) - \gamma_7 \frac{C_o(\mathbf{x})}{C_o(\mathbf{x}) + \gamma_6} \right)$$

$$u_1^i = \frac{\alpha_0 C_o(\mathbf{x}_i) + (\beta_5 - \alpha_0 C_o(\mathbf{x}_i))w_3^i}{\alpha_1 + \alpha_0 C_o(\mathbf{x}_i) + \beta_4 w_2^i} \quad u_2^i = \frac{\alpha_2\alpha_3 c_1 u_1^i(1 - w_1^i)}{1 + \alpha_4 + \alpha_2\alpha_3 c_1 u_1^i - \alpha_4 w_1^i}$$

$$u_4^i = \frac{\beta_0 C_o(\mathbf{x}_i)}{\beta_1 + \beta_0 C_o(\mathbf{x}_i)}$$

The next question is how to solve these equations. The geometry of a two-dimensional domain is as shown in Fig. 1.27, wherein the size of the cells is exaggerated.

The computational algorithm can be summarized as follows—for details see [22].

1. Solve the extracellular equation on a regular grid, using an Alternating-Direction Implicit (ADI) method for the partial differential equation, lagging the secretion term.
2. Interpolate cAMP from the grid to the cell positions and update the intracellular variables and the secretion by an implicit scheme.
3. Update cell movement. If a cell is not moving, should it begin to move? If so, compute the direction and start movement. If it is moving, should it continue?
4. Transfer the secreted cAMP to the grid and repeat the cycle.

Two examples of the wave patterns in aggregation predicted by the model are shown in Fig. 1.28. These are certainly qualitatively consistent with the experimentally-observed waves in Fig. 1.3.

What do the analysis and computations of the continuum and cell-based models explain and predict? Some of these are discussed here—for others see the original literature cited above.

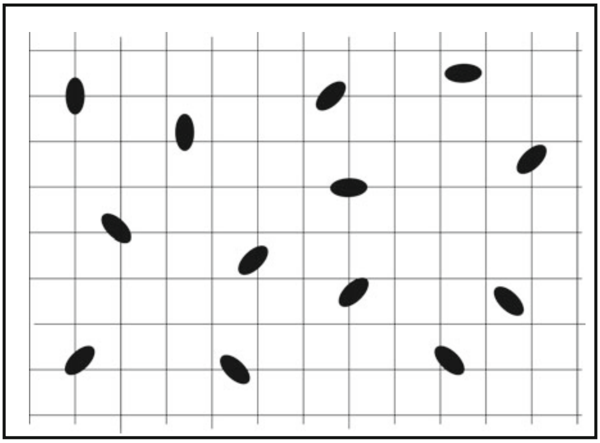

Fig. 1.27 The computational grid for the aggregation problem. The *black ellipses* represent the cells, but not to scale

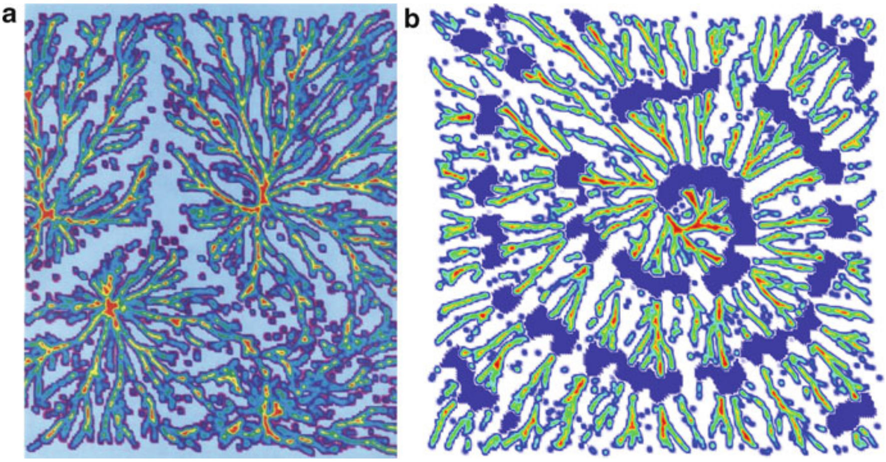

Fig. 1.28 Aggregation waves. On the *left* is shown a large field in which several pacemakers organize local aggregation patterns. On the *right* is the spiral cAMP wave (*dark blue*) superimposed on the cell streams. Note that in both images some cells are *left* behind. The time evolution of these patterns shows that cells always move toward the highest local concentration of cAMP, which leads to the observed streams

- A single cell can be a pacemaker. This is not addressed herein, but is done in [29].
- The continuum model predicts the effect of density and cell excitability on the frequency of oscillation, the wave speed, and the size of the central core.
- The cell-based model provides an explanation for the origin of streaming and the origin of spiral waves: computations show that cell movement and random variations in cell density are necessary for streaming and facilitate the generation of spirals.
- The model predicts that cells must choose a direction within 10–15 s in order to orient to the local gradient.
- Computations show that aggregation is very robust with respect to the choice of direction of movement.

Of course the model for cAMP production is not correct in detail—experiments since its formulation have contributed greatly to our understanding of the signal transduction network leading to cAMP production, but the input-output behavior is quantitatively correct, and thus all questions that depend only on this can be addressed. As we show here and in the original papers, the exterior problem dealing with aggregation can be addressed and the predictions are quite accurate. One major factor that is missing is the cell-cell interaction that occurs when cells make contact. This is addressed in the following section.

1.6 Multicellular Problems

Collective cell motion occurs in the streaming, mound and slug stages of Dd [74], as well as in vertebrate embryos [106]. In Dd streams this involves small numbers of cells, but the slug is composed of about 10^5–10^6 cells (cf. Fig. 1.29). Weijer et al. [31] have developed techniques to visualize the effects of signal-transduction

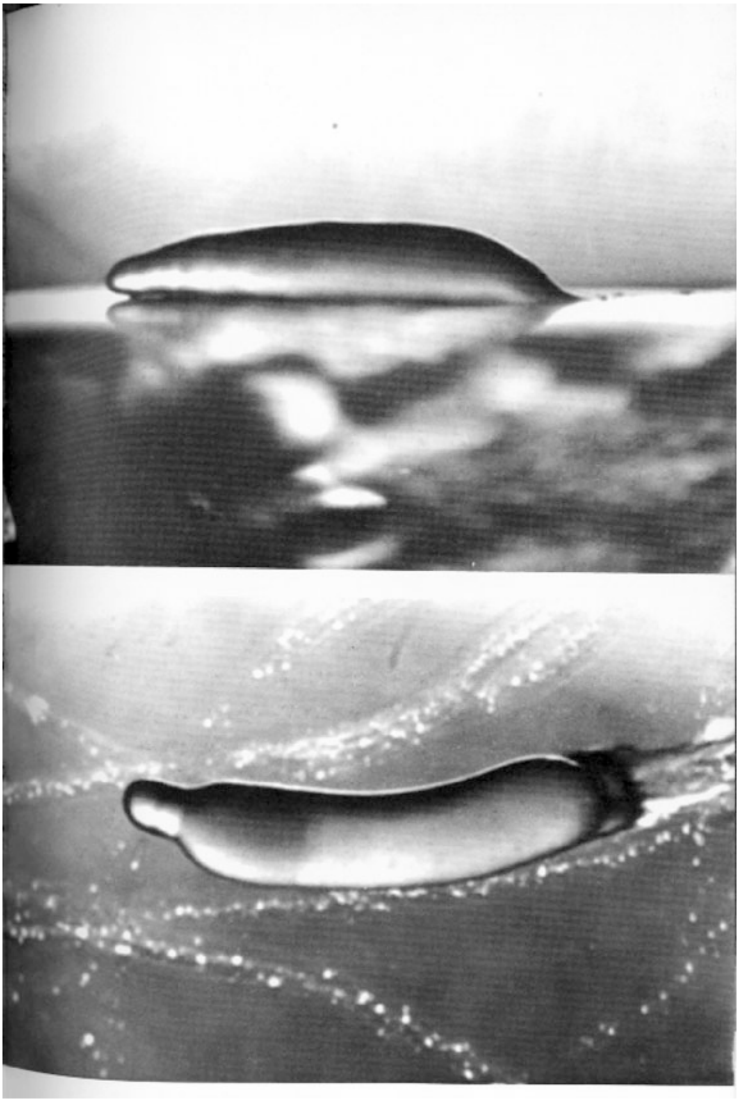

Fig. 1.29 A side and top view of a Dd slug gliding on a substrate

at the single cell level, by imaging the fluorescence from GFP-tagged PHds in response to cAMP signals. They record the movement of individual cells in three dimensions, and find that when wild-type cells are imaged in aggregation streams, their movement is very much like that of cells moving as individuals, despite the fact that new adhesion systems are expressed at this stage. The cells in the center of the stream tend to move slightly faster than those at the edge.

Mixing mutants lacking myosin II with wild type cells has shed light on the role of myosin II in multicellular motility. Mutants lacking myosin II accumulate at the edges of aggregation streams and the back of the slug, and become distorted by their adhesive interaction with wild-type cells [109]. There are two adhesion systems, characterized as A and B, expressed during the aggregation stage, and either or both may be responsible for excluding the myosin II null cells. Xu et al. postulate that mhcA$^-$ cells cannot generate sufficient protrusive force to disrupt contacts between adherent cells in streams, but can enter streams where the cells are weakly adherent [109].

The motion of Dd slugs is mechanically very similar to the motion of single cells. Vardy et al. [100] show that the slug leaves behind cell prints in the slime sheath as it migrates. The cell prints are either parabolic or elliptic in shape. Because the cell prints are sharp, i.e. exhibit no smearing near their boundary, they speculate that the cells that make up the prints are temporarily stationary and secrete a “traction protein” that allows the slug to adhere to the substratum. It is not known whether these traction proteins are related to integrins or contact proteins, but the underlying mechanics of the motion of a slug is conceptually similar to single cell motion. As will be clear later, similar computational techniques will apply in the two cases. We begin with a description of a single cell.

1.6.1 The Mechanics of a Single Cell

As will be clear from the previous sections, the movement of an individual cell involves the integration of numerous processes, and to incorporate all of these into a realistic model of a deformable cell is overly ambitious at this point. In particular, the details of how actin networks are reorganized under the membrane in response to extracellular signals is a complex process that is only partially understood, and it is not feasible to incorporate the level of detail required to describe this in a multicellular model at present. However, it may be possible to understand aspects of tissue motion, in particular that of the Dd slug, with a relatively simple mechanical model of a cell. This has been done in [24, 75], and a schematic of the cell model is shown in Fig. 1.30. In the approach taken in previous work, the opposite extreme in descriptions is adopted; cells are treated as incompressible viscoelastic solids and their stress-strain response characteristics are lumped into three elements that coincide with the three major axes. Along each axis the stress-strain behavior is described by a nonlinear version of a standard Kelvin element, as shown in Fig. 1.30. Since there is an elastic element in each branch the immediate response to a step

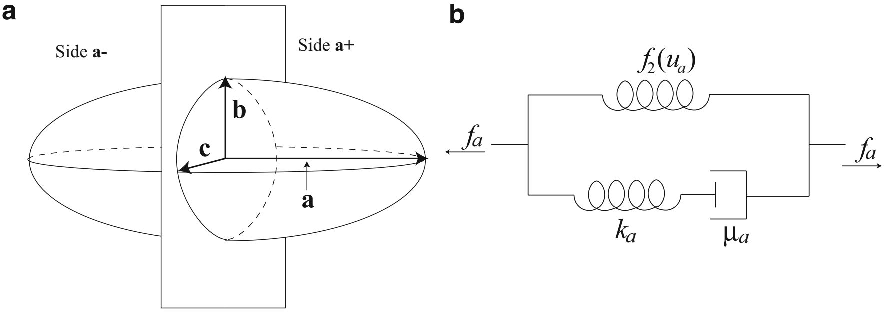

Fig. 1.30 A schematic of the model cell and the element of a standard *solid*, or Kelvin element along each axis of the ellipsoid. It consists of a nonlinear spring in parallel with a Maxwell element, which comprises a linear spring in series with a dashpot

change in the applied force is a step change in displacement in the elastic elements, followed by slower flow in the viscous element. Release of the external forces leads to a return to the rest length of the element, and since we assume that the elements are identical along the three axes, the equilibrium shape is spherical.

This is a reasonable first description, since the cytoplasm in many amoeboid cells has been characterized as a viscoelastic material whose properties are dominated by actin filaments and microtubules. However, the elastic modulus of actin solutions is concentration dependent [64], and they exhibit strain hardening [110], a property that may be important in slug movement.

When the cell deforms due to interactions with other cells or an obstacle, the three deformations are not arbitrary, because we stipulate that the total volume of the cell must be conserved.[3] In [75] the constant volume constraint was satisfied by first computing the deformation and then correcting the change in all radii so as to correct the volume.

In the computational algorithm we can decompose the total stress on an ellipsoid into the shear along the axes of the ellipsoid and an additional 'isotropic' part reflected in a pressure that constrains the overall deformation so as to satisfy the constraint that the volume remains constant. In a continuum description of an incompressible material this pressure serves as a Lagrange multiplier that forces satisfaction of the incompressibility condition. In [24] and what follows here the pressure is the deviation from a rest state and therefore may have either sign: a negative pressure causes the cell to compress and a positive pressure causes the cell to expand.

---

[3] This may not be true in reality, and we could allow small changes without changing the results. Osmotic fluxes may well change the total volume during deformations, but this has not been characterized experimentally, and incorporating it would add a great deal of complexity for an as yet unquantifiable increase in accuracy.

The equation governing the length of an axis of a cell is

$$u_a' = \left(\frac{k_a}{\mu_a} [f_a(t) + \bar{p} - f_2(u_a)] + f_a'(t) \right) \left(\frac{df_2(u_a)}{du_a} + k_a \right)^{-1}, \tag{1.24}$$

where u_a is the change in the length of the **a** axis, f_2 is the force from the spring in parallel, μ_a is the viscous coefficient of the dashpot, k_a is the spring constant for the spring in the Maxwell element, f_a is the magnitude of the force applied at each end in opposite directions, and $\bar{p}$ is the force due to pressure. There are three such equations one for each axis and one equation due to the volume constraint given by

$$0 = {u_a}'(u_b + b_0)(u_c + c_0) + (u_a + a_0){u_b}'(u_c + c_0) + (u_a + a_0)(u_b + b_0){u_c}', \tag{1.25}$$

where a_0, b_0, and c_0 are the initial lengths of the cell axes. This system of ordinary differential equations determines the shape of a cell and is solved numerically.

1.6.2 The Multicell Problem

Suppose there are N cells in an aggregate, sufficiently close so that at least some cells may be in contact. The forces that a cell may be subject to are classified as follows [24].

- Active forces $\mathbf{T}_{i,j}$ a cell exerts on neighboring cells or the substrate: the reaction force to this is denoted $\mathbf{M}_{j,i}$.
- The reaction to forces exerted by other cells on it.
- Dynamic drag forces that arise as a moving cell forms and breaks adhesive bonds with neighboring cells.
- Static frictional forces that exist when cells are rigidly attached to each other or to the substrate.

We let $\mathcal{N}_i^a$ denote the neighbors, including the substrate, of i upon which a cell can exert traction. The ‘neighbor’ relation is symmetric for all cells; if cell i can exert traction on cell j, then cell j can exert traction on cell i, but not true for the substrate, which is passive in that it does not generate stress. The motive force that i generates is

$$\mathbf{M}_i = \sum_{j \in \mathcal{N}_i^a} \mathbf{M}_{j,i},$$

and the total traction force which other cells exert on it is

$$\mathbf{T}_i = \sum_{j \in \mathcal{N}_i^a} \mathbf{T}_{j,i}.$$

The *dynamic friction force* on cell i due to interaction with j is defined as

$$\mathbf{D}_{j,i} = \mu_{ij}(v_j - \mathbf{v}_i),$$

where μ_{ij} is the friction coefficient, which is symmetric. Thus, the total dynamic friction force on cell i, due to the set $\mathcal{N}_i^d$ of cells that interact with i via a frictional force, is

$$\mathbf{D}_i = \sum_{j\in\mathcal{N}_i^d} \mathbf{D}_{j,i} = \sum_{j\in\mathcal{N}_i^d} \mu_{ij}(\mathbf{v}_j - \mathbf{v}_i).$$

By definition, statically-bound cells function as one rigid object, so that if i is bound to j and j is bound to k, then i is bound to k. In particular, if i is statically bound to the substrate either directly or indirectly then it can transmit forces applied to it to the substrate. These are the only type of chains that can transmit stress from the interior; a chain of say four cells statically bound to each other but not bound to the substrate simply functions as a larger unit. If S_{ji} denotes the static binding force on the ith cell when bound to the jth, then $S_{ji} = -S_{ij}$ and the cell-cell forces cancel on all but those cells attached to the substrate. Let $\mathcal{N}_i^s$ denote the set of cells that statically bind to cell i; then the total force on the ith cell is the sum of all the foregoing, viz.,

$$\begin{aligned}\mathbf{F}_i &= \mathbf{M}_i + \mathbf{T}_i + \mathbf{D}_i + \sum_{j\in\mathcal{N}_i^s} \mathbf{S}_{ji} \qquad (1.26)\\ &= \sum_{j\in\mathcal{N}_i^a} \mathbf{M}_{j,i} + \sum_{j\in\mathcal{N}_i^a} \mathbf{T}_{j,i} + \sum_{j\in\mathcal{N}_i^d} \mu_{ij}(\mathbf{v}_j - \mathbf{v}_i) + \sum_{j\in\mathcal{N}_i^s} \mathbf{S}_{ji}.\end{aligned}$$

If we sum these over all cells we see that the sum of the tractions and motive forces, as well as sum of the dynamic friction force, vanish for all cell-cell interactions in the interior of the slug. The surviving terms are those due to direct interaction of a cell with the substrate, or the indirect interaction via a chain of statically-connected cells that is connected to the substrate. The latter takes the form of a force on an interior cell equal and opposite to the traction force it exerts on a statically-connected chain of cells. Thus in the absence of static binding there is no mechanism by which an interior cell can transmit stress to the boundary, and accordingly, there can be no volumetric forces on the slug in a continuum description in the absence of other mechanisms.

In any case, one has to define precisely how cells exert forces on one another, how to model the active forces, the drag forces, etc. This is a rather involved process, the details of which are given in [24], and will not be repeated here. The computational algorithm defined in [24, 75] proceeds as follows.

Step 1. Locate all cells that are within a given distance from cell i.
Step 2. Search the cell's neighborhood to determine if the cAMP levels are above threshold, and if so find the direction of the highest cAMP concentration.

Step 3. If necessary, orient the cell towards the direction of the highest cAMP concentration.

Step 4. Find all the forces that act on the cell, $\mathbf{F}^{net}$ from each of the neighbor cells found in Step 1, deform the three axes of the ellipsoid, and move the cell according to (2).

Figure 1.31 shows one example of the aggregation patterns that results from the application of this algorithm. This simulation is done with 2500 cells, but the cAMP output of each computational cell is equivalent to that of 16 real cells (see [75] for details). Similar results are obtained with 10K cells and a fourfold reduction of their cAMP output. In these simulations, it was assumed that the cAMP distribution is uniform in the z direction, which is sufficiently accurate during early aggregation, because the cell distribution is essentially 2D, but for mound formation

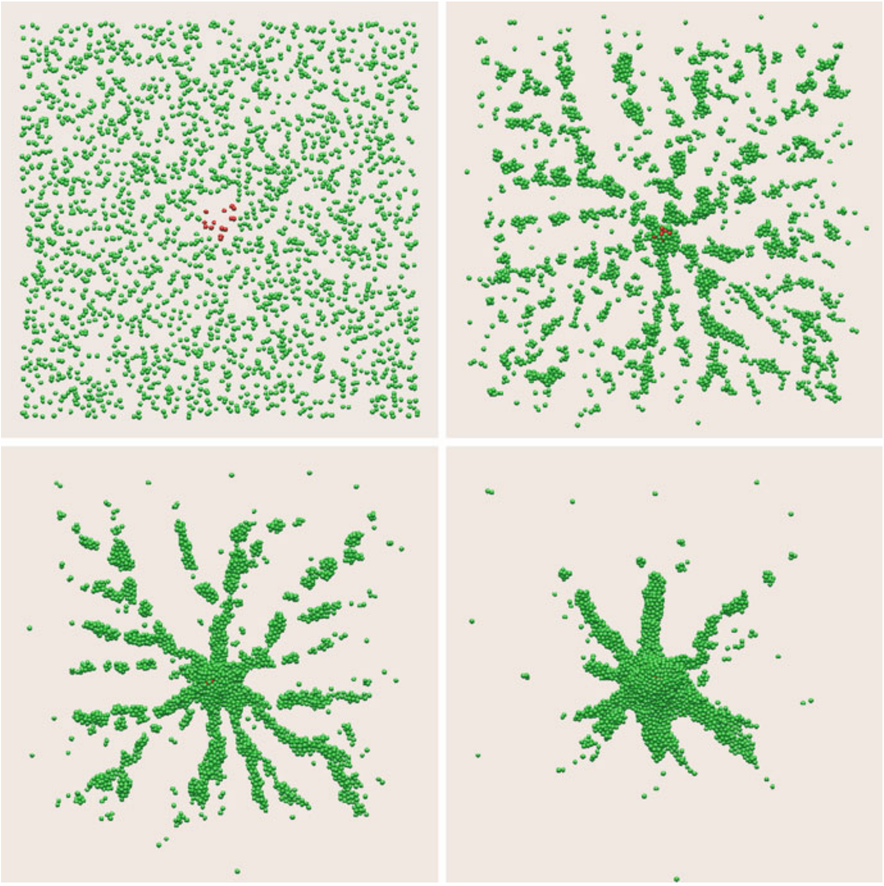

Fig. 1.31 The early aggregation pattern, driven by pacemakers (*red*) in the center of a field of cells. The times beginning at the *upper left*, are 0, 80, 160, and 320 min. From [75], with permission

and movement of the slug a 3D computation is needed. However, Fig. 1.32 shows that the initial stages of mound formation results when cells at the center are pushed upward by the inward movement of the outer cells.

The similarity with the patterns that emerge when the cells are treated as particles and their movement governed by formal rules, as in Fig. 1.28 (left), is evident. However the more detailed treatment of the mechanics allows for more realistic comparisons between the theoretical predictions and the experimental results.

For example, Bonner [7] discovered how to produce two-dimensional slugs that are only one cell layer thick and migrate between a glass slide and a drop of mineral oil. In Fig. 1.33 we show the computational equivalent of this experiment with a 2D slug whose movement is driven by pacemaker cells at the front. In the upper left panel another group of pacemaker cells is introduced at the side, and subsequent frames show how this pacemaker organizes a secondary slug which then breaks away. This also occurs in Bonner's 2D slugs, although there the new pacemaker arises spontaneously, presumably due to variations in properties of the cells, whereas in the computational experiment the second pacemaker is imposed. Aside from this, the results are quite similar.

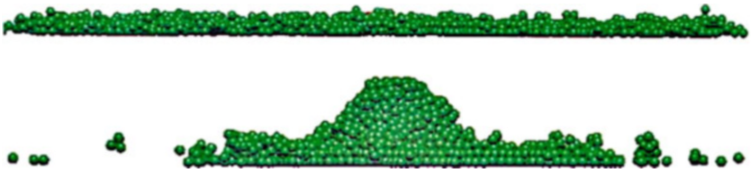

Fig. 1.32 A cross-sectional view of the aggregation field at 80 (*top*) and 320 (*bottom*) min. From [75], with permission

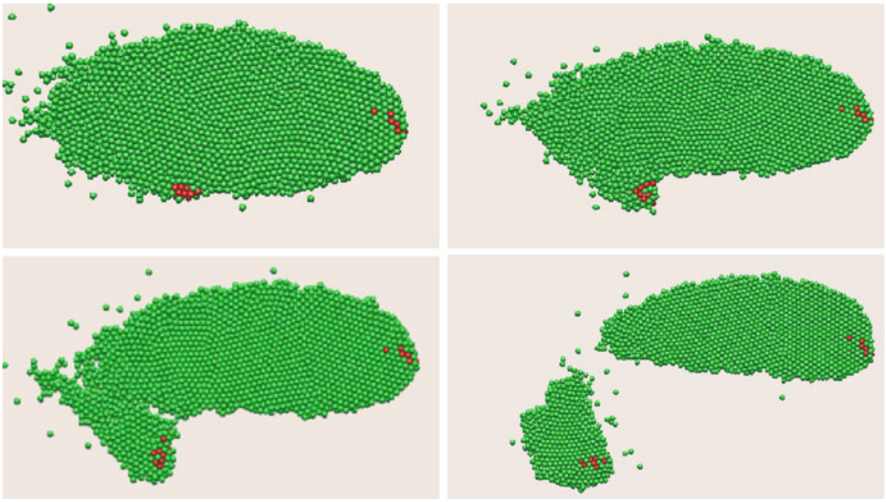

Fig. 1.33 A migrating 2D slug with an auxiliary pacemaker. From [75], with permission

Detailed modeling of the later stages of slug movement is very complicated because a slug can frequently elevate the leading one third of the slug as if to sample the environment, and then touch down again, thus moving in a pulsatile motion. During migration, cAMP waves propagate down the length of the slug [30] and cells begin to differentiate into pre-stalk and pre-spore cells that eventually become the stalk and spore cells in the next stage of the life cycle, the fruiting body. How the proportions of cell types are determined is a long-standing question [77], and some of the complexities of slug stage movement and patterning are discussed in the work of Weijer and collaborators [78, 102, 104]. We shall not pursue this further, but for one final question.

1.6.3 Who Does the Work in the Slug?

According to our earlier discussion of the mechanics, if our description of cell interactions properly accounts for cell-cell and cell-substrate interactions, then cells in the interior of the slug can only contribute to movement of the slug if there is a chain of rigidly-connected cells that attaches to the substrate. In [24] this is called the bedspring model, since the rigid cells form a network that transmits stress to the boundary and allows other cells to crawl through it. This is similar to what occurs when a single cell migrates through a tissue, but in order for this mechanism to work in the Dd slug, the network must be dynamic and cells must be able to "freeze" when stress is applied, but also to move. Beautiful experiments in which the total force exerted by a slug was measured on a rotating table seemed to indicate that the motive force scales with the number of cells in the slug, rather than the number in contact with the substrate [50, 51]. These experiments motivated a computational study of which cells provide the motive force in the slug. Using an extension of the cell-based model described in the previous section, a large number of simulations were done using different aspect ratios of the slugs [24]. The initial configurations ranged through 250 cases having from 1 to 5 cells in the width and height, and from 1 to 10 cells in the length of the slug. In all cases the cells were stimulated to move in a fixed direction by a traveling wave. The results are shown in Fig. 1.34. It is clear from the left panel that the force scales with the number of cells in contact with the surface, but the right panel suggests how one could conclude that it scales with the volume of the slug. There the force generated by slugs having the same ratio of volume to area in contact with the surface fall on a straight line, but the slope varies with that ratio. Thus if this ratio was approximately constant in the experiments one could conclude that the force scale with the volume.

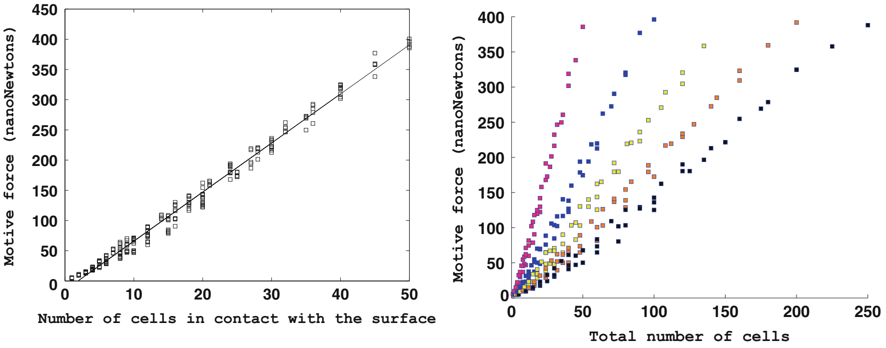

Fig. 1.34 Data from 250 different simulations for the translational force of the slug in nanoNewtons (*vertical axis*) and the number of cells in contact with the surface (*left*), or the total number of cells in the slug (*right*) (*horizontal axis*). Five lines are clear in the *right panel*—these correspond to subsets of the data in which the initial height of the slug is held constant, which implies that the volume of the slug and the surface area in contact with the substrate are proportional. From [24] with permission

1.7 Conclusion

In these notes we have attempted to describe a number of interesting problems connected with cell motility and to indicate some aspects on which progress toward understanding them has been made. Hopefully the reader will have gained some insight into the role of mathematical modeling and analysis in the resolutions of these problems, but will also recognize that much is yet to be done. We are in fact a long way from a complete understanding of cell motility, either from the experimental side, where experiments can shed light on specific processes, or from the mathematical side, where the interactions of the underlying processes can only be understood through mathematical modeling and computational analysis.

Appendix: Singular Perturbation Reduction

We know how to express reaction dynamics as the evolution equation

$$\frac{dx}{dt} = f(x, p) \tag{1.27}$$

where $x \in M \subseteq R^n$ and $p \in R^p$. Suppose there is a separation of variables into those that vary rapidly and those that change slowly on the chosen time scale. This leads to a system of equations of the form

$$\begin{aligned} \frac{dx}{dt} &= f(x, y, \epsilon, p) \\ \epsilon\frac{dy}{dt} &= g(x, y, \epsilon, p) \end{aligned} \tag{1.28}$$

wherein ϵ is a small parameter and x (resp., y) is a slow (resp., fast) variable on the t time scale.

- What are the implications of this separation for understanding the dynamics?
- More precisely, can we use the separation of time scales to reduce the dimensionality of the problem we have to analyze?

The following simple example will illustrate some of the underlying ideas. Consider the reaction

$$A \xrightarrow{k_1} B \xrightarrow{k_2} C, \tag{1.29}$$

where A, B, and C are generic chemical species. We assume mass action kinetics and first-order reactions and therefore can write the governing equations as

$$\begin{aligned} \dot{x} &= k_1 x \\ \dot{y} &= k_1 x - k_2 y \\ \dot{z} &= k_2 y. \end{aligned} \tag{1.30}$$

where x, y, and z stand for the concentration of A, B, and C, resp. In addition we have the conservation condition

$$(x + y + z)(t) = (x + y + z)(0). \tag{1.31}$$

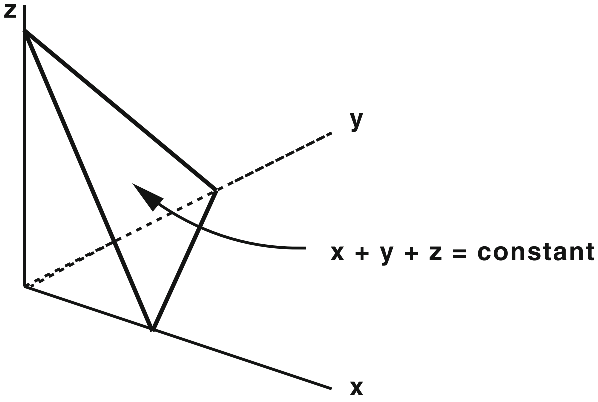

Clearly A and B will disappear completely in the steady state, and the exact solution for the transient problem for A and B is

$$\begin{aligned} x &= x_0 e^{-k_1 t} \\ y &= y_0 e^{-k_2 t} + \frac{k_1 x_0}{k_2 - k_1}[e^{-k_1 t} - e^{-k_2 t}]. \end{aligned}$$

If $k_2 \gg k_1$, then after a time $t \sim \mathcal{O}(1/k_2)$ we have

$$y(t) \sim \frac{k_1 x_0 e^{-k_1 t}}{k_2} = \frac{k_1}{k_2} x(t).$$

But this is what we would get directly if we set $\dot{y} = k_1 x - k_2 y = 0$ since then

$$y = \frac{k_1 x}{k_2}.$$

This is what we call the 'pseudo-steady-state' or PSS value of y , (or alternatively, the 'quasi-steady-state' QSS value of y), and the hypothesis that we can do this is called the 'pseudo-(or quasi) steady-state hypothesis'—the PSSH or QSSA. Can we justify setting $\dot{y} = 0$ analytically, and how do we understand it geometrically?

To formalize this reduction, consider the system

$$\frac{dx}{d\tau} = f(x, y) \tag{1.32}$$

$$\epsilon \frac{dy}{d\tau} = g(x, y),$$

where $x \in R^n$, $y \in R^m$, and $\epsilon > 0$ is a small parameter.

Let $y = \phi(x)$ be one of the solutions of the system

$$g(x, y) = 0 \tag{1.33}$$

defined on a closed bounded domain $D \subset R^n$. The *degenerate or slow system* associated with (1.33) and the solution $y = \phi(x)$ is the system

$$\frac{dx}{d\tau} = f(x, \phi(x)). \tag{1.34}$$

The solution $y = \phi(x)$ is said to be *isolated* on D if there exists an $\eta > 0$ such that (1.33) has no solution other than ϕ with the property that

$$\|y - \phi(x)\| < \eta.$$

The associated *adjoined (or fast) system* is

$$\frac{dy}{ds} = g(x^*, y), \tag{1.35}$$

where x^* is regarded as a parameter.

- The isolated solution $y = \phi(x)$ is said to be *positively stable* in D if for all x^* in D the points $y = \phi(x^*)$ are asymptotically stable stationary points, in the sense of Lyapunov, of the adjoined system.
- The *domain of influence* of an isolated, positively stable $y = \phi(x)$is the set of points (x^*, y^*) such that the solution of the adjoined system with the initial conditions $y(0) = y^*$ tends to $\phi(x^*)$ as $s \to \infty$.

One of the earliest formal statements of what is now know as a singular perturbation reduction is given by *Tikhonov's theorem* [99].

Theorem 2 *If some root $y = \phi(x)$ of $g = 0$ is an isolated, positively stable root in some bounded closed domain D, if the initial point $(x(0),\ y(0))$ belongs to the domain of influence of this root, and if the solution of the degenerate system belongs to D for $0 \le t \le T$, then the solution $(x(t,\epsilon), y(t,\epsilon))$ of the original system tends to the solution $(\bar{x}(t), \bar{y}(t))$ of the degenerate or slow system , as ϵ approaches 0, the passage to the limit*

$$\lim_{\epsilon \to 0} y(t,\epsilon) = \bar{y}(t) = \phi(\bar{x}, t)$$

holding for $0 < t \le T^0 < T$, and the passage to the limit

$$\lim_{\epsilon \to 0} x(t,\epsilon) = \bar{x}(t)$$

holding for $0 \le t \le T^0 < T$.

The geometry behind the theorem is qualitatively as shown in the following sketch.

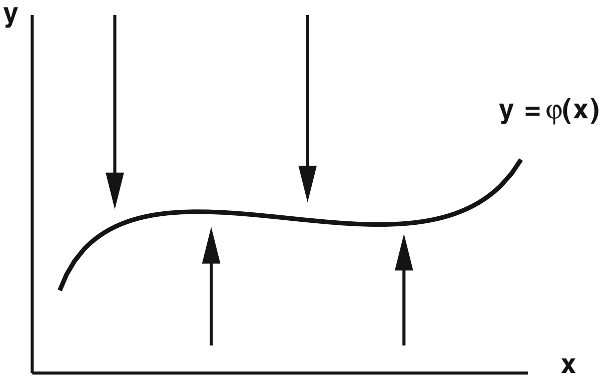

Remarks

1. This can be generalized to allow ϵ and t dependence in the right-hand side of the DE.
2. If y is sufficiently close to $\phi(x)$ then on the fast time scale this analysis can be viewed in the framework of center manifold theory.
3. There are many variations on the theme and many expositions of it.

1.8 Glossary

Actin is one of the most abundant proteins found in eukaryotic cells and is highly conserved throughout evolution. Actin monomers polymerize in an ATP-dependent process to form polarized actin filaments. The helical actin filament has a barbed end and a pointed end. In non-muscle cells, the dynamic organization of filamentous actin gives rise to various cell structures, such as filopodia, lamellipodia, and stress fibers.

AKT/PKB Cellular homologue of AKT retroviral oncogene protein Ser/Thr kinase. Also called Protein Kinase B because of homology with Protein Kinase A and Protein Kinase C family members. AKT has an amino-terminal pleckstrin homology (PH) domain that binds to the lipid products of phosphoinositide 3-kinase, phosphatidylinositol-3,4-bisphosphate and phosphatidylinositol-3,4,5-trisphosphate. This binding locates it at the plasma membrane where it becomes phosphorylated on Thr-308 (human AKT1) in the activation loop of the catalytic domain by phosphoinositide-dependent kinase 1 (PDK1). This phosphorylation leads to activation. Full activation requires phosphorylation at a second site (Ser-473 of human AKT). Mammals have at least three distinct genes for AKT family members (AKT1, AKT2 and AKT3) and they appear to at least partially redundant in function.

Alpha-actinin is an actin cross-linking protein that belongs to the spectrin superfamily. It forms antiparallel homodimers in a rod-like structure with one actin-binding domain on each side of the rod. It can, therefore, cross-link two filaments of actin.

Arp2/3 (Actin-related protein complex) Extracellular and intracellular signals that initiate actin cytoskeletal rearrangements flow through the Arp2/3 complex. The Arp2/3 complex is composed of seven subunits, two unconventional actin proteins, Arp2 and Arp3, and five additional proteins. One copy of each subunit is present in the complex. In addition to contributing to the nucleation of actin filaments, the Arp2/3 complex caps the slow-growing pointed ends of actin filaments and promotes the elongation of the actin filament at the fast-growing barbed end. Arp2/3 complexes are localized at the branch point of two different filaments, binding to both the side of the mother filament and the pointed end of the daughter filament. These interactions create an approximate 70° angle with the actin barbed end oriented towards the plasma membrane. These observations serve as the basis for the “dendritic nucleation” model in which Arp2/3, through its interaction with F-actin, is a key regulator of the unique meshwork of F-actin in the lamellipodial structure. The Arp2/3 complex influences the strictly regulated reorganization of the actin cytoskeleton in response to various signaling pathways.

B-Raf is a serine/threonine protein kinase that is a member of the Raf family of protein kinases. Raf-B can be activated by the small GTPase Ras as well as Rap1. cAMP activates MAP-Kinase through B-Raf.

Cdc42 is a Rho-family GTPase that was first identified as a regulator of cell polarity and budding in yeast. In mammalian cells, Cdc42 is activated in response to integrins and bradykinin. Activated Cdc42 induces formation of actin-rich structures known as filopodia. Cdc42 affects actin directly by binding to its effector WASP, an activator of Arp2/3 and actin polymerization. During cell migration, Cdc42 is also responsible for polarization of the cell.

Chemotaxis the directed movement of a microorganism or cell in response to a chemical stimulus.

G-proteins G-proteins are heterotrimeric proteins comprising alpha, beta and gamma subunits. When bound to guanine nucleotide diphosphate (GDP), G-proteins are inactive, and are activated when bound to guanine nucleotide triphosphate (GTP). When activated, they split into alpha-GTP and beta-gamma subunits that are separately used for control of downstream processes. The alpha subunit has intrinsic hydrolysis activity that removes a phosphate group, whereupon the alpha-GDP subunit recombines with a beta-gamma subunit.

G-protein coupled receptors (GPCRs) G-protein-coupled receptors are integral membrane proteins with seven membrane-spanning helices. G-protein is bound to the receptor in its inactive state, and when a ligand is bound, the receptor may undergo a conformational change that facilitates the GDP-GTP exchange on a G protein, which then detaches from the receptor. GPCRs can desensitize when exposed to ligand for a sufficient length of time as a result of phosphorylation of a cytoplasmic receptor domain by protein kinases.

In vitro the recreation of biological processes in an artificial laboratory environment.

In vivo biological processes that take place within a living organism or cell.

Kinase an enzyme that catalyzes addition of a phosphoryl group to proteins.

MLCK (Myosin Light Chain kinase) is a serine/threonine kinase that phosphorylates the regulatory light chain (RLC) of the molecular motor myosin, resulting in increased contraction. In nonmuscle cells MLCK is involved in the regulation of cell motility.

MLCP (Myosin Light Chain phosphatase) dephosphorylates the regulatory light chain of molecular motor myosin, thus inactivating it. MLCP is involved in the regulation of the actin cytoskeleton and cell spreading.

PAK (p21-activated kinase) is a serine/threonine kinase that binds to and is activated by Rho family GTPases. The PAK family of kinases is highly conserved among species. PAK family members have an N-terminal kinase domain and a C-terminal p21 Rac and Cdc-42-binding domain. The binding of Rho family GTPases to the C-terminus of PAK causes a conformational change resulting in autophosphorylation and activation of the kinase. PAK family members have been shown to play a role in actin polymerization and cytoskeletal dynamics.

PI3K Phosphoinositide 3-kinase catalyzes the phosphoryation of phosphatidylinositol-4,5-bisphosphate to produce phosphatidylinositol-3,4,5-trisphosphate. The enzyme is cytosolic and become localized to the plasma membrane, which activates the catalytic subunit. Binding of the catalytic subunit to activated Ras appears to enhance the membrane association and activation.

Phosphatase an enzyme that removes the phosphoryl group from proteins.

Protease (proteinase, proteolytic enzyme) an enzyme that degrades proteins, such as collagen, laminin, and fibrin.

PTEN is a phosphatase that can dephosphorylate the lipid products or phosphoinositide 3-kinase, especially phosphatidylinositol-3,4,5-trisphosphate. By dephosphorylating these lipids, PTEN attenuates signaling via the phosphoinositide 3-kinase pathway.

Rac is a small GTP-binding protein which belongs to the Ras superfamily. Rac activity depends on the ratio of GTP/GDP bound forms. GEFs (guanine nucleotide exchange factors), GAPs (GTPase activating proteins) and GDIs (guanine nucleotide dissociation inhibitors) thus determine its activity by regulating of the GTP/GDP bound form. The downstream effectors of Rac are involved in regulation of the cytoskeleton.

Ras is a small protein that is activated by exchange proteins of the SOS (Son of Sevenless) or Ras-GRF (Ras GDP Releasing Factor) family. The release of GDP and binding of GTP 'activates' Ras, allowing it to bind to downstream effectors, including phosphoinositide 3-kinase (PI3K). Ras is anchored at the plasma membrane via a carboxy-terminal farnesyl group. One function of Ras is to facilitate localization of its cytosolic effectors at the plasma membrane. Mutant forms of Ras that stabilize the GTP bound state contribute to tumor formation.

Rho GTPase is a member of Rho family of small GTP binding proteins, which include Rho A, B, G. It is active in the GTP-bound state and inactive when bound to GDP. Activation of Rho results in its association with a wide variety of effector molecules and leads to activation of downstream signaling cascades. Rho proteins exhibit intrinsic GTPase activity Rho that is significantly stimulated by GTPase activating proteins (GAPs). Conversely, GTP exchange factors (GEFs) promote exchange of GDP for GTP, thus activating Rho. Rho GTPase regulates actin cytoskeleton organization and assembly, in particular actin stress fibers and focal adhesion formation. It is involved in cellular processes that depend on actin cytoskeleton such as cell spreading and migration.

RLC (Regulatory Light Chain of myosin) binds to the neck region of Heavy Chain (HC) of myosin and regulates its motor activity. When RLC is phosphorylated by myosin light chain kinase on Ser19 it causes conformational changes in myosin and activates its motor function. Dephosphorylation of RLC by myosin light chain phosphatase negatively regulates myosin activity. Phosphorylation of RLC in smooth muscle cells leads to initiation of contraction, whereas in striated muscles it increases speed and force of contractions. There is also evidence that in nonmuscle cells myosins are participating in cell motility, spreading, cytokinesis and vesicle transport.

ROCK Rho kinase/ROKalpha/ROCK-II and a related protein p160ROCK/ ROCK-I are serine/threonine kinases. Integrin-dependent activation of Rho family small GTPases induces Rho-Rho kinase interaction and facilitates translocation of Rho kinase to the cell membrane. Rho kinase facilitates formation of focal adhesions and actin stress fiber assembly. It cooperates with other Rho effectors to regulate the formation of actin structures. Rho kinase associates with and phosphrylates myosin phosphatase. Phosphorylation leads to the inhibition of phosphatase activity and thereby enhances myosin-mediated contractility. Rho kinase has been shown to facilitate tumor cell invasion due to its role in cytoskeletal reorganization. In addition, Rho kinase promotes cytokinesis by phosphorylation of myosin light chain at the cleavage furrow.

Small G proteins A class of monomeric, low molecular weight (20–25 kDa) GTP-binding proteins that regulate a variety of intracellular processes. The GTP bound form of the protein is active and is inactivated by an intrinsic GTPase activity, which is controlled by GTPase activators (GAPs), GDP dissociation inhibitors (GDIs), and guanine nucleotide exchange factors (GEFs).

SOS (Son of Sevenless) is an exchange factor that stimulates GDP release from Ras to allow GTP binding and formation of the active state. SOS has a pleckstrin homology (PH) domain that mediates binding to the membrane.

WASP (The Wiskott-Aldrich Syndrome protein) mediates a variety of signals from kinases, receptors, and small G proteins to the Arp2/3 complex and the actin cytoskeleton. Homologs in the WASP family include SCAR and WAVE. The family members share two similar domains: one that mediates interactions of WASP with adaptor proteins such as profilin, and another involved in interaction with Arp2/3 complex and G-actin. GTP-Cdc42 binding to WASP stimulates the Arp2/3 complex resulting in actin polymerization.

References

1. B. Alberts, A. Johnson, J. Lewis, M. Raff, K. Roberts, P. Walter, *Molecular Biology of the Cell*, 4th edn. (Garland Science, New York, London, 2002)
2. U. Alon, M.G. Surette, N. Barkai, S. Leibler, Robustness in bacterial chemotaxis. Nature **15**, 168–171 (1999)
3. R. Ananthakrishnan, A. Ehrlicher, The forces behind cell movement. Int. J. Biol. Sci. **3**(5), 303–17 (2007)
4. L. Blanchoin, T.D. Pollard, Hydrolysis of ATP by polymerized actin depends on the bound divalent cation but not profilin. Biochemistry **41**(2), 597–602 (2002)
5. D. Boal, *Mechanics of the Cell* (Cambridge University Press, Cambridge, 2002)
6. J.T. Bonner, *The Cellular Slime Molds* (Princeton University Press, Princeton, NJ, 1967)
7. J.T. Bonner, A way of following individual cells in the migrating slugs of Dictyostelium discoideum. Proc. Natl. Acad. Sci. **95**(16), 9355–9359 (1998)
8. D. Bray, *Cell Movements: From Molecules to Motility* (Garland Publishing, New York, 2001)

9. T. Bretschneider, K. Anderson, M. Ecke, A. Müller-Taubenberger, B. Schroth-Diez, H.C. Ishikawa-Ankerhold, G. Gerisch, The three-dimensional dynamics of actin waves, a model of cytoskeletal self-organization. Biophys. J. **96**(7), 2888–2900 (2009)
10. J.A. Brzostowski, C.A. Parent, A.R. Kimmel, A Gα-dependent pathway that antagonizes multiple chemoattractant responses that regulate directional cell movement. Genes Dev. **18**, 805–15 (2004)
11. B. Bugyi, M.F. Carlier, Control of actin filament treadmilling in cell motility. Annu. Rev. Biophys. **39**, 449–470 (2010)
12. L. Cai, A.M. Makhov, D.A. Schafer, J.E. Bear, Coronin 1B antagonizes cortactin and remodels arp2/3-containing actin branches in lamellipodia. Cell **134**(5), 828–842 (2008)
13. Y. Cao, H. Li, L. Petzold, Efficient formulation of the stochastic simulation algorithm for chemically reacting systems. J. Chem. Phys. **121**(9), 4059–67 (2004)
14. M. Carlier, D. Pantaloni, E. Korn, The effects of Mg2+ at the high-affinity and low-affinity sites on the polymerization of actin and associated ATP hydrolysis. J. Biol. Chem. **261**, 10785–10792 (1986)
15. L.B. Case, C.M. Waterman, Adhesive F-actin waves: a novel integrin-mediated adhesion complex coupled to ventral actin polymerization. PLoS One **6**(11), e26631 (2011)
16. M.Y. Chen, R.H. Insall, P.N. Devreotes, Signaling through chemoattracnt receptors in *Dictyostelium*. Trends Genet. **12**(2), 52–57 (1996)
17. H. Chen, B.W. Bernstein, J.R. Bamburg, Regulating actin-filament dynamics in vivo. Trends Biochem. Sci. **25**(1), 19–23 (2000). Review
18. Y. Cheng, H.G. Othmer, A model for direction sensing in *dictyostelium discoideum*: Ras activity and symmetry breaking driven by a $g_{\beta\gamma}$- mediated, $g_{\alpha2}$-ric8 – dependent signal transduction network. PLoS Comput. Biol. **12**, e1004900 (2016)
19. C.Y. Chung, S. Funamoto, R.A. Firtel, Signaling pathways controlling cell polarity and chemotaxis. Trends Biochem. Sci. **26**(9), 557–566 (2001). Review
20. J. Condeelis, A. Bresnick, M. Demma, S. Dharmawardhane, R. Eddy, A.L. Hall, R. Sauterer, V. Warren, Mechanisms of amoeboid chemotaxis: an evaluation of the cortical expansion model. Dev. Genet. **11**(5–6), 333–340 (1990)
21. L.P. Cramer, M. Siebert, T.J. Mitchison, Identification of novel graded polarity actin filament bundles in locomoting heart fibroblasts: implications for the generation of motile force. J. Cell Biol. **136**(6), 1287–1305 (1997)
22. J.C. Dallon, H.G. Othmer, A discrete cell model with adaptive signalling for aggregation of dictyostelium discoideum. Philos. Trans. R. Soc. Lond. B Biol. Sci. **352**(1351), 391–417 (1997)
23. J.C. Dallon, H.G. Othmer, A continuum analysis of the chemotactic signal seen by *dictyostelium discoideum*. J. Theor. Biol. **194**(4), 461–483 (1998)
24. J.C. Dallon, H.G. Othmer, How cellular movement determines the collective force generated by the dictyostelium discoideum slug. J. Theor. Biol. **231**, 203–222 (2004)
25. P. Dancker, L. Hess, Phalloidin reduces the release of inorganic phosphate during actin polymerization. Biochim. Biophys. Acta **1035**(2), 197–200 (1990)
26. L.A. Davidson, R.E. Keller, Neural tube closure in xenopus laevis involves medial migration, directed protrusive activity, cell intercalation and convergent extension. Development **126**(20), 4547–4556 (1999)
27. P.N. Devreotes, T.L. Steck, Cyclic $3', 5'$ AMP relay in *Dictyostelium discoideum* II. Requirements for the initiation and termination of the response. J. Cell Biol. **80**, 300–309 (1979)
28. P.N. Devreotes, P.L. Derstine, T.L. Steck, Cyclic $3', 5'$ AMP relay in *Dictyostelium discoideum* I. A technique to monitor responses to controlled stimuli. J. Cell Biol. **80**, 291–299 (1979)
29. G. DeYoung, P.B. Monk, H.G. Othmer, Pacemakers in aggregation fields of *Dictyostelium disc oideum*. Does a single cell suffice? J. Math. Biol. **26**, 486–517 (1988)
30. D. Dormann, C.J. Weijer, Propagating chemoattractant waves coordinate periodic cell movement in dictyostelium slugs. Development **128**(22), 4535–4543 (2001)

31. D. Dormann, G. Weijer, C.A. Parent, P.N. Devreotes, C.J. Weijer, Visualizing PI3 kinase-mediated cell-cell signaling during dictyostelium development. Curr. Biol. **12**(14), 1178–1188 (2002)
32. R.A. Firtel, R. Meili, Dictyostelium: a model for regulated cell movement during morphogenesis. Curr. Opin. Genet. Dev. **10**(4), 421–427 (2000). Review
33. P. Friedl, K. Wolf, Tumour-cell invasion and migration: diversity and escape mechanisms. Nat. Rev. Cancer **3**(5), 362–74 (2003)
34. I. Fujiwara, S. Takahashi, H. Tadakuma, S. Ishiwata, Microscopic analysis of polymerization dynamics with individual actin filaments. Nat. Cell. Biol. **4**(9), 666–673 (2002)
35. C. Gadgil, C.H. Lee, H.G. Othmer, A stochastic analysis of first-order reaction networks. Bull. Math. Biol. **67**, 901–946 (2005)
36. C.W. Gardiner, *Handbook of Stochastic Methods* (Springer, Berlin, Heildeberg, 1983)
37. G. Gerisch, Chemotaxis in dictyostelium. Annu. Rev. Physiol. **44**(1), 535–552 (1982)
38. G. Gerisch, U. Wick, Intracellular oscillations and release of cyclic AMP from *Dictyostelium* cells. Biochem. Biophys. Res. Commun. **65**, 364–370 (1975)
39. G. Gerisch, D. Hulser, D. Malchow, U. Wick, Cell communication by periodic cyclic amp pulses. Philos. Trans. R. Soc. Lond. **272**, 181–192 (1975)
40. G. Gerisch, T. Bretschneider, A. Muler-Taubenberger, E. Simmeth, M. Ecke, S. Diez, K. Anderson, Mobile actin clusters and traveling waves in cells recovering from actin depolymerization. Biophys. J. **87**(5), 3493–3503 (2004)
41. D.T. Gillespie, A general method for numerically simulating the stochastic time evolution of coupled chemical reactions. J. Comput. Phys. **22**, 403–434 (1976)
42. D.T. Gillespie, Exact stochastic simulation of coupled chemical reactions. J. Phys. Chem. **81**(25), 2340–2361 (1977)
43. A.R. Gingle, Critical density for relaying in *Dictyostelium discoideum* and its relation to phosphodiesterase secretion into the extracellular medium. J. Cell Sci. **20**, 1–20 (1976)
44. A.L. Hall, A. Schlein, J. Condeelis, Relationship of pseudopod extension to chemotactic hormone-induced actin polymerization in amoeboid cells. J. Cell Biol. **37**(3), 285–299 (1988)
45. B. Heit, S. Tavener, E. Raharjo, P. Kubes, An intracellular signaling hierarchy determines direction of migration in opposing chemotactic gradients. J. Cell Biol. **159**(1), 91–102 (2002)
46. J. Hu, H.G. Othmer, A theoretical analysis of filament length fluctuations in actin and other polymers. J. Math. Biol. **63**(6), 1001–1049 (2011)
47. J. Hu, A. Matzavinos, H.G. Othmer, A theoretical approach to actin filament dynamics. J. Stat. Phys. **128**(1–2), 111–138 (2007)
48. J. Hu, H.W. Kang, H.G. Othmer, Stochastic analysis of reaction–diffusion processes. Bull. Math. Biol. **76**, 854–894 (2014)
49. M. Iijima, Y.E. Huang, P. Devreotes, Temporal and spatial regulation of chemotaxis. Dev. Cell **3**(4), 469–478 (2002). Review
50. K. Inouye, Measurement of the motive force of the migrating slug of dictyostelium discoideum by a centrifuge method. Protoplasma **121**, 171–177 (1984)
51. K. Inouye, I. Takeuchi, Analytical studies on migrating movement of the pseudoplasmodium of *Dictyostelium Discoideum*. Protoplasma **99**, 289–304 (1979)
52. R.H. Insall, O.D. Weiner, PIP3, PIP2, and cell movement–similar messages, different meanings? Dev. Cell. **1**(6), 743–747 (2001)
53. C. Janetopoulos, T. Jin, P. Devreotes, Receptor-mediated activation of heterotrimeric G-proteins in living cells. Science **291**(5512), 2408–2411 (2001)
54. P.A. Janmey, Mechanical properties of cytoskeletal polymers. Curr. Opin. Cell Biol. **2**, 4–11 (1991)
55. T. Jin, N. Zhang, Y. Long, C.A. Parent, P.N. Devreotes, Localization of the G protein $\beta\gamma$ complex in living cells during chemotaxis. Science **287**(5455), 1034–1036 (2000)
56. H.W. Kang, L. Zheng, H.G. Othmer, A new method for choosing the computational cell in stochastic reaction–diffusion systems. J. Math. Biol. **60**, 1017–1099 (2012)
57. H.W. Kang, L. Zheng, H.G. Othmer, A new method for choosing the computational cell in stochastic reaction-diffusion systems. J. Math. Biol. **60**, 1017–1099 (2012)

58. V. Khamviwath, J. Hu, H.G. Othmer, A continuum model of actin waves in dictyostelium discoideum. PloS One **8**(5), e64272 (2013)
59. A.R. Kimmel, C.A. Parent, The signal to move: D. discoideum go orienteering. Science **300**(5625), 1525–1527 (2003)
60. J.R. Kuhn, T.D. Pollard, Real-time measurements of actin filament polymerization by total internal reflection fluorescence microscopy. Biophys. J. **88**(2), 1387–1402 (2005)
61. D.A. Lauffenburger, A.F. Horwitz, Cell migration: a physically integrated molecular process. Cell **84**, 359–369 (1996)
62. A. Levchenko, P.A. Iglesias, Models of eukaryotic gradient sensing: application to chemotaxis of amoebae and neutrophils. Biophys. J. **82**(1 Pt 1), 50–63 (2002)
63. L. Limozin, M. Barmann, E. Sackmann, On the organization of self-assembled actin networks in giant vesicles. Eur. Phys. J E **10**(4), 319–330 (2003)
64. F.C. MacKintosh, Theoretical models of viscoelasticity of actin solutions and the actin cortex. Biol. Bull. **194**(3), 351–353 (1998). No abstract available
65. A. Matzavinos, H.G. Othmer, A stochastic analysis of actin polymerization in the presence of twinfilin and gelsolin. J. Theor. Biol. **249**(4), 723–736 (2007)
66. J.L. McGrath, E.A. Osborn, Y.S. Tardy, C.F. Dewey Jr, J.H. Hartwig, Regulation of the actin cycle in vivo by actin filament severing. Proc. Natl. Acad. Sci. USA **97**(12), 6532–7 (2000)
67. S. McLaughlin, J. Wang, A. Gambhir, D. Murray, PIP_2 and proteins: interactions, organization and information flow. Annu. Rev. Biophys. Biomol. Struct. **31**, 151–175 (2002). Review
68. R. Meili, C. Ellsworth, S. Lee, T.B. Reddy, H. Ma, R.A. Firtel, Chemoattractant-mediated transient activation and membrane localization of akt/PKB is required for efficient chemotaxis to cAMP in dictyostelium. EMBO J. **18**(8), 2092–2105 (1999)
69. H. Meinhardt, Orientation of chemotactic cells and growth cones: models and mechanisms. J. Cell Sci. **17**(17), 2867–2874 (1999)
70. R. Melki, S. Fievez, M.F. Carlier, Continuous monitoring of pi release following nucleotide hydrolysis in actin or tubulin assembly using 2-amino-6-mercapto-7-methylpurine ribonucleoside and purine-nucleoside phosphorylase as an enzyme-linked assay. Biochemistry **35**(37), 12038–45 (1996)
71. T.J. Mitchison, L.P. Cramer, Actin-based cell motility and cell locomotion. Cell **3**, 371–379 (1996). Review. No abstract available
72. F. Oosawa, S. Asakura, *Thermodynamics of the Polymerization of Protein* (Academic, New York, 1975)
73. H.G. Othmer, A graph-theoretic analysis of chemical reaction networks (1979). Lecture Notes, Rutgers University. Available at www.math.umn.edu/~othmer/graphrt.pdf
74. H.G. Othmer, P. Schaap, Oscillatory cAMP signaling in the development of dictyostelium discoideum. Comments Theor. Biol. **5**, 175–282 (1998)
75. E. Palsson, H.G. Othmer, A model for individual and collective cell movement in *dictyostelium discoideum*. Proc. Natl. Acad. Sci. **97**, 11448–11453 (2000)
76. C.A. Parent, P.N. Devreotes, A cell's sense of direction. Science **284**(5415), 765–770 (1999). Review
77. E. Pate, H.G. Othmer, Differentiation, cell sorting and proportion regulation in the slug stage of *Dictyostelium discoideum*. J. Theor. Biol. **118**, 301–319 (1986)
78. M. Pineda, C. Weijer, R. Eftimie, Modelling cell movement, cell differentiation, cell sorting and proportion regulation in dictyostelium discoideum aggregations. J. Theor. Biol. **370**, 135–150 (2015)
79. T.D. Pollard, Regulation of actin filament assembly by arp2/3 complex and formins. Annu. Rev. Biophys. Biomol. Struct. **36**, 451–477 (2007)
80. T.D. Pollard, L. Blanchoin, R.D. Mullins, Molecular mechanisms controlling actin filament dynamics in nonmuscle cells. Annu. Rev. Biophys. Biomol. Struct. **29**(1), 545–76 (2000)
81. A.Y. Pollitt, R.H. Insall, WASP and SCAR/WAVE proteins: the drivers of actin assembly. J. Cell Sci. **122**(Pt 15), 2575–2578 (2009). doi:10.1242/jcs.023879

82. R.K. Raman, Y. Hashimoto, M.H. Cohen, A. Robertson, Differentiation for aggregation in the cellular slime molds: the emergence of autonomously signalling cells in *Dictyostelium discoideum*. J. Cell. Sci. **21**, 243–259 (1976)
83. D. Raucher, T. Stauffer, W. Chen, K. Shen, S. Guo, J.D. York, M.P. Sheetz, T. Meyer, Phosphatidylinositol 4,5-bisphosphate functions as a second messenger that regulates cytoskeleton-plasma membrane adhesion. Cell **100**(2), 221–228 (2000)
84. J. Rosenblatt, P. Peluso, T.J. Mitchison, The bulk of unpolymerized actin in xenopus egg extracts is ATP-bound. Mol. Biol. Cell **6**(2), 227–36 (1995)
85. K.R. Sanft, H.G. Othmer, Constant-complexity stochastic simulation algorithm with optimal binning. J. Chem. Phys. **143**(8), 074108 (2015)
86. P. Schaap, Evolutionary crossroads in developmental biology: dictyostelium discoideum. Development **138**(3), 387–396 (2011)
87. D. Sept, J. Xu, T.D. Pollard, J.A. McCammon, Annealing accounts for the length of actin filaments formed by spontaneous polymerization. Biophys. J. **77**(6), 2911–2919 (1999)
88. M.P. Sheetz, D. Felsenfeld, C.G. Galbraith, D. Choquet, Cell migration as a five-step cycle. Biochem. Soc. Symp. **65**, 233–43 (1999)
89. F. Siegert, C.J. Weijer, Analysis of optical density wave propagation and cell movement in the cellular slime mould *Dictyostelium discoideum* **49**, 224–232 (1991)
90. J.V. Small, Microfilament-based motility in non-muscle cells. Curr. Opin. Cell Biol. **1**, 75–79 (1989)
91. J.V. Small, T. Stradal, E. Vignal, K. Rottner, The lamellipodium: where motility begins. Trends Cell Biol. **12**(3), 112–120 (2002). Review
92. D.R. Soll, The use of computers in understanding how animal cells crawl, in *International Review of Cytology*, vol. 163, ed. by K.W. Jeon, J. Jarvik (Academic, New York, 1995), pp. 43–104
93. P.A. Spiro, J.S. Parkinson, H.G. Othmer, A model of excitation and adaptation in bacterial chemotaxis. Proc. Natl. Acad. Sci. **94**(14), 7263–7268 (1997)
94. T.M. Svitkina, G.G. Borisy, Arp2/3 complex and actin depolymerizing factor/cofilin in dendritic organization and treadmilling of actin filament array in lamellipodia. J. Cell Sci. **145(5)**, 1009–26 (1999)
95. J. Swanson, D.L. Taylor, Local and spatially coordinated movements in *D*ictyostelium discoideum amoedae during chemotaxis. Cell **28**, 225–232 (1982)
96. Y. Tang, H.G. Othmer, A G protein-based model of adaptation in *Dictyostelium discoideum*. Math. Biosci. **120**(1), 25–76 (1994)
97. Y. Tang, H.G. Othmer, Excitation, oscillations and wave propagation in a G-protein-based model of signal transduction in Dictyostelium discoideum. Philos. Trans. R. Soc. Lond. B Biol. Sci. **349**(1328), 179–95 (1995)
98. J.A. Theriot, T.J. Mitchison, Actin microfilament dynamics in locomoting cells. Nature **352**(6331), 126–131 (1991)
99. A. Tikhonov, Systems of differential equations containing small parameters multiplying derivatives. Math. Sb. **31**, 575–586 (1952)
100. P.H. Vardy, L.R. Fisher, E. Smith, K.L. Williams, Traction proteins in the extracellular matrix of *Dictyostelium discoideum* slugs. Nature **320**(6062), 526–529 (1986)
101. B. Varnum, K.B. Edwards, D.R. Soll, *Dictyostelium* amebae alter motility differently in response to increasing versus decreasing temporal gradients of cAMP. J Cell Biol. **101**, 1–5 (1985)
102. B. Vasiev, C.J. Weijer, Modelling of dictyostelium discoideum slug migration. J. Theor. Biol. **223**, 347–59 (2003)
103. J.B. Wallingford, L.A. Niswander, G.M. Shaw, R.H. Finnell, The continuing challenge of understanding, preventing, and treating neural tube defects. Science **339**(6123), 1222002 (2013)
104. C.J. Weijer, Signalling during dictyostelium development, in *Dictyostelids* (Springer, Berlin, 2013), pp. 49–70

105. D. Wessels, J. Murray, D.R. Soll, Behavior of *Dictyostelium* amoebae is regulated primarily by the temporal dynamic of the natural cAMP wave. Cell Motil. Cytoskeleton **23**(2), 145–156 (1992)
106. L. Wolpert, R. Beddington, T. Jessel, P. Lawrence, E. Meyerowitz, J. Smith, *Principles of Development* (Oxford University Press, Oxford, 2002)
107. B. Wurster, K. Schubiger, U. Wick, G. Gerisch, Cyclic GMP in *Dictyostelium discoideum*: oscillations and pulses in response to folic acid and cyclic AMP signals. FEBS Lett. **76**, 141–144 (1977)
108. X. Xin, H.G. Othmer, A trimer of dimers- based model for the chemotactic signal transduction network in bacterial chemotaxis. Bull. Math. Biol. **74**, 2339–2382 (2012)
109. X.S. Xu, A. Kuspa, D. Fuller, W.F. Loomis, D.A. Knecht, Cell-cell adhesion prevents mutant cells lacking myosin II from penetrating aggregation streams of dictyostelium. Dev. Biol. **175**(2), 218–226 (1996)
110. J. Xu, Y. Tseng, D. Wirtz, Strain hardening of actin filament networks. regulation by the dynamic cross-linking protein alpha-actinin. J. Biol. Chem. **275**(46), 35886–35892 (2000)
111. S.H. Zigmond, Recent quantitative studies of actin filament turnover during locomotion. Cell Motil. Cytoskeleton **25**, 309–316 (1993)